Geochimica et Cosmochimica Acta 342 (2023) 198–214

Contents lists available at ScienceDirect

Geochimica et Cosmochimica Acta

journal homepage: www.elsevier.com/locate/gca

Germanium speciation in experimental and natural sphalerite: Implications for critical metal enrichment in hydrothermal Zn-Pb ores

Weihua Liu [a,*], Yuan Mei [a], Barbara Etschmann [b], Matthew Glenn [a], Colin M. MacRae [a], Sam C. Spinks [a], Chris G. Ryan [a], Joël Brugger [b], David J. Paterson [c]

[a] CSIRO Mineral Resources, Clayton, VIC 3168, Australia
[b] School of Earth, Atmosphere and the Environment, Monash University, Clayton, VIC 3800, Australia
[c] Australia Synchrotron, ANSTO, Clayton, VIC 3168, Australia

ARTICLE INFO

Article history:
Received 12 August 2022
Accepted 30 November 2022
Available online 02 December 2022
Associate editor: Martin Reich

Keywords:
Germanium
Critical minerals
Sediment-hosted Zn-Pb deposits
Hydrothermal deposits
XANES
SXRF
XFM
Synchrotron
Trace element

ABSTRACT

The critical metal germanium (Ge) is recovered as a by-product of mining other commodities, such as zinc and thermal coal. We investigated the Ge incorporation mechanism in sphalerite synthesized under hydrothermal conditions like those of sediment-hosted Zn-Pb deposits. Sphalerite ± galena ± barite formed via reactions of Ge ± Fe ± Cu ± Ba-bearing brine with calcite and reduced sulfur at 200 °C and water vapor-saturated pressure. The products were examined using backscattered electron (BSE) imaging, electron probe microanalysis (EPMA), electron backscattered diffraction (EBSD), synchrotron X-ray fluorescence (SXRF) and micro-X-ray absorption near-edge structure (μ-XANES). We show that Ge(IV) is incorporated into sphalerite and bonded with reduced sulfur, both in the experimental sphalerite and in natural zinc ore samples from the MacArthur River Zn-Pb-Ag deposits, Australia. Copper K-edge XANES spectra show that copper occurs as Cu(I) in the experimental sphalerite, consistent with previous studies on Cu in natural sphalerite. The experiments reveal that Ge(IV) substitution in sphalerite occurs with and without the presence of other metal ions (e.g., Cu(I)), indicating that Ge(IV) substitution can be accommodated via charge balance by vacancies as well as by coupled substitution in the synthesized sphalerite. *Ab initio* quantum chemical simulations confirm that sphalerite can readily accommodate Ge, with the crystal structure and average Zn-S, Zn-Zn, S-S distances retained when replacing > 3 mol% of the Zn sites with Ge(IV), Ge(II), Cu(I) or Fe(II), demonstrating the resilience and flexibility of the sphalerite crystal structure. These Ge incorporation mechanisms explain the previous observations of multiple ways of Ge incorporation in natural sphalerite. The study provides experimental and molecular simulation insights for understanding the processes related to the formation and extraction of Ge in zinc ores.

1. Introduction

Germanium (Ge) is listed as a critical mineral by major countries (USGS, 2020; Mudd et al., 2018). Many critical mineral resources are recovered as a by-product of mining and processing for other principal elements (Nassar et al., 2015). For example, Ge, indium (In), and gallium (Ga), which are widely and increasingly used in electronic and optoelectronic devices, are recovered as by-products from refining zinc ores (Keller and Anderson, 2018). One of the scientific challenges to enabling the mining of critical minerals as a by-product of major commodities is understanding the distribution of these elements at deposit-to-mineral scales; this is controlled by geochemical processes that lead to the incorporation of trace elements into the principal host minerals. Such knowledge helps characterize the resource potential of a deposit and is required for the targeted extraction of valuable metals in an economically and environmentally sustainable manner.

Sediment-hosted Zn-Pb deposits are a favorable host to critical metals such as Ge. The formation of such deposits ranges from syngenetic exhalative to epigenetic replacement during regional fluid flow (e.g., Cooke et al., 2000, Brugger et al., 2003; Leach et al., 2010), but Ge is most abundant in the epigenetic sediment-hosted Zn deposits compared to other Zn deposit types (Bernstein, 1985), implying Ge is mainly brought in during post-sedimentary hydrothermal activities. Recently, an epigenetic carbonate replacement model has been proposed for the formation of the super-giant carbonate-hosted Zn-Pb-Ag deposits of the MacArthur River (HYC), Australia, with elevated Ge concentrations up to ~40 ppm in sphalerite (Spinks et al., 2021).

* Corresponding author.
E-mail address: weihua.liu@csiro.au (W. Liu).

https://doi.org/10.1016/j.gca.2022.11.031
0016-7037/

Sphalerite (ZnS) is notable for hosting a variety of trace elements including Ga, Ge, In, Ag, Cd, Co, Cu, Fe and Mn (e.g., Cook et al., 2009; George et al., 2016; Pring et al., 2020; Cugerone et al., 2020), and a sphalerite thermometer has been proposed based on an empirical relationship between Ga, Ge, In, Fe and Mn concentrations with fluid inclusion homogenization temperatures from different Zn deposits (Frenzel et al., 2016). The distribution and speciation of Ge in natural sphalerite have been studied extensively, and there is consensus that Ge exists mainly in lattice substitution sites for Zn(II) in sphalerite (e.g., Cook et al., 2015; Belissont et al., 2016; Goldmann et al., 2019). Most studies suggest that natural sphalerite contains only Ge(IV) and that Ge-incorporation is coupled with monovalent elements such as Cu(I) and Ag(I) (Johan, 1988; Belissont et al., 2014) or lattice vacancies (e.g., Cook et al., 2015; Belissont et al., 2016). Germanium(IV) is the dominant form of Ge in other minerals/rocks. Belissont et al., (2019) and Etschmann et al., (2017) identified tetrahedrally-coordinated Ge(IV) in chalcopyrite from various locations, and our previous study revealed the predominance of organic Ge(IV)-complexes in Ge-bearing coals (Etschmann et al., 2017). The similarity between Ge(IV) and Si(IV) has led to the use of the Ge/Si ratio as a tracer to study geothermal waters (e.g., Evans and Derry, 2002), clay minerals (e.g., Perez-Fodich and Derry, 2020) and water-silicate interactions at ambient temperatures (Fernandez et al., 2021). To date the only reported direct evidence of Ge(II) in terrestrial rocks is Bonnet et al.'s (2017) study showing that sphalerite from Mississippi Valley-Type epigenetic deposits in Tennessee (USA) contains both Ge(II) and Ge(IV).

This study aims to test the proposed mechanisms of the incorporation and oxidation state of Ge in natural hydrothermal sphalerite, using a combination of experimental, computational, and micro-characterization techniques. In particular, the proposed charge balance by vacancies is difficult to assess in natural sphalerites due to the fact they usually contain many trace elements. Hydrothermal synthesis with known starting composition can effectively isolate the interference of trace elements. We select the experimental method used by Liu et al., (2021), since their experimental conditions and produced mineral assemblages and textures are similar to those found in sediment-hosted Zn-Pb deposits. The experiments were conducted at 200 °C and water vapor-saturated pressure and designed to assess the impact of solution composition (e.g., Cu, Fe and initial Ge oxidation state) on Ge incorporation into sphalerite under the simulated ore-forming conditions. The nature of Ge in the synthetic sphalerite was compared to that in sphalerites from the HYC deposit. The composition of the samples was characterized using electron probe micro-analysis (EPMA); their mineralogy and textures via Electron backscatter diffraction (EBSD); and Ge-distribution and -oxidation state were mapped using synchrotron X-ray fluorescence (SXRF) and micro-X-ray absorption near-edge structure (μ-XANES) techniques, respectively. Finally, *ab initio* quantum chemical calculations were conducted to investigate Ge substitution in sphalerite at an atomic level. The key questions to be answered are 1) what is the oxidation state of Ge in the synthesized hydrothermal sphalerite formed under conditions similar to the sediment-hosted Zn-Pb deposits? And 2) is a coupled substitution with other trace elements (e.g., Cu) necessary for charge balance when Ge(IV) is incorporated into sphalerite?

2. Methods

2.1. Hydrothermal sphalerite synthesis experiments

Ge-bearing sphalerite was hydrothermally synthesized at 200 °C and water-saturated pressure in Teflon-lined stainless-steel autoclaves (Liu et al., 2021). To test the impact of different oxidation states, Ge(II) bromide ($GeBr_2$) and Ge(IV) oxide (GeO_2) in powder form, were used as the Ge source. Note that $GeBr_2$ was used instead of $GeCl_2$ due to the volatility of the latter. Cu(I) and Fe(II) chlorides were also added to some experiments to test the impact of Fe and Cu in solution. All the chemicals were analytical grade, bought from Merck. The sample compositions are compiled in Table 1.

Native sulfur (S) was used as the sulfur source in the experiments, as native sulfur disproportionates in water to produce both reduced sulfur (H_2S) and sulfate (SO_4^{2-}) at temperatures above 120 °C (Ellis and Giggenbach, 1971):

$$4S + 4H_2O = 3H_2S + 2H^+ + SO_4^{2-} \quad (1)$$

Thermodynamic calculations using Geochemist's Workbench modeling package (Bethke, 2007) show that the pH values of typical experimental solutions (3 molal (*m*) NaCl, 0.35 *m* S) are around 2.1 at 200 °C. The presence of calcite increased the solution pH to 3.8–6.3 (Table 1), Reaction (1) also conveniently buffers the redox state near the sulfide/sulfate boundary at the experimental temperature of 200 °C, evidenced by the precipitation of both sulfide and sulfate minerals (see Results section). This is in line with conditions observed in many sediment-hosted zinc deposits, e.g., Red Dog barite and Zn-Pb deposits in Alaska (Kelley and Jennings, 2004; Kelley et al., 2004), and most Mississippi Valley-Type deposits (sulfates such as barite, celestine; rare and only minor occurrence of pyrrhotite, e.g., Leach et al., 2010). Note that the concentration of Ge, Fe and Cu is small compared to that of S, therefore the disproportionation of S buffers the system redox condition.

For each experiment, about 10 ml of Zn + Ge ± Cu ± Fe ± Ba-bearing NaCl solutions were loaded into an autoclave together with ~0.1 g native sulfur and 0.3 g of calcite. The autoclaves then were placed in a fan-forced oven and heated to 200 ± 1 °C. After two days at this temperature, all the native sulfur had been converted to sulfate and sulfide. All experimental runs lasted 2–3 weeks to ensure the completion of the reactions. A temperature of 200 °C for the reaction was chosen because it is within the range estimated for the ore-formation in typical SEDEX (100–150 °C) and MVT and Irish Type (84–250 °C) Zn-Pb deposits (Wilkinson, 2014). The relatively high temperature helps the reaction proceed faster than at lower temperatures. After the experiments, the autoclaves were cooled with a fan for ~30 min to room temperature. The solution was then retrieved for pH measurement and concentration analysis of selected elements (Table 1) using Inductively coupled plasma optical emission spectroscopy (ICP-OES). The solid products were washed with distilled water and dried under ambient conditions before the micro-characterizations described below.

2.2. SEM and EBSD

Solid samples were examined in the SEM in both "as produced" form and cross-sections. A FEI Quanta 400, field emission, environmental scanning electron microscope (SEM) was used. For the "as produced" samples, dried crystals were sprinkled onto double-sided conductive carbon tape and examined in the SEM in low vacuum mode with a chamber vacuum of 0.5 torr, a beam energy of 15 keV and probe current of approximately 0.8 nA. Backscattered electron (BSE) Images showing the morphology of the reacted samples were collected, since this highlights the different minerals. Initial phase identification was performed using energy-dispersive X-ray spectrometry (EDS) analyses.

For EBSD analyses, the samples were mounted in Struers' Epofix epoxy resin and polished using standard metallographic techniques to 50 nm colloidal SiO_2 finish. Final surface preparation was performed using a Technoorg Linda SEM prep 2000 Ar ion

Table 1
Composition of initial sample solutions and pH measured with a Mettler Toledo® pH meter and an Inlab® Expert Pro ISM Sensor at 25 °C before and after experiment. The final elemental concentrations of the resultant solutions at 25 °C were also shown (measured with Inductively Coupled Plasma-Optical Emission Spectrometry (ICP-OES)).

Sample ID	G2	G4	G6	G8	G9
Initial Composition	0.02 m GeO_2 + 0.02 m CuCl + 0.07 m $ZnCl_2$ + + 0.4 m S + 3 m NaCl + calcite	0.02 m $GeBr_2$ + 0.02 m CuCl + 0.07 m $ZnCl_2$ + 0.3 m S + 3 m NaCl + calcite	0.02 m $GeBr_2$ + 0.04 m CuCl + 0.1 m $BaCl_2$ + $PbCl_2$ + 0.07 m $ZnCl_2$ + 0.3 m S + 0.3 m NaCl + calcite	0.02 m $GeBr_2$ + 0.01 m $FeCl_2$ + 0.07 m $ZnCl_2$ + 0.3 m S + 0.3 m NaCl + calcite	0.02 m $GeBr_2$ + 0.1 m $BaCl_2$ + 0.01 m $PbCl_2$ + 0.07 m $ZnCl_2$ + 0.3 m S + 0.3 m NaCl + calcite
Initial pH@25 °C (acidified by HCl)	2.26	2.26	2.28	2.28	2.28
pH@25 °C after experiment	5.87	4.97	3.78	6.32	6.14
Cu (final, mg/L)	2	12	7	–	–
Fe (final, mg/L)	–	–	–	0.2	–
Ge (final, mg/L)	120	260	230	990	1140
Na (final, g/L)	79.4	80.6	8.2	8.5	6.7
Pb (final, mg/L)	<1	<1	3	<0.1	<1
Zn (final, mg/L)	66	16	8	0.4	<2

beam polisher operated at ion beam energies ranging from 10 kV to 400 V to progressively reduce the damage induced by the ion beam. These samples were coated with approximately 4 nm of carbon in a Leica EM ACE600 carbon coater. EBSD analysis was done at a beam energy of 20 keV and a probe current of approximately 1.2–3.4nA using a Bruker e⁻Flash EBSD system. Maps were collected overnight using diffraction patterns of 160 × 120 pixels (10 × 10 binning), a Hough transform of 99 × 99 pixels, and dwell times ranging from 20 to 100 ms per pixel. Map sizes were 1024 × 884 pixels and pixel sizes were 310 nm for lower magnification maps and 77 nm for higher magnification maps. EDS spectra from each pixel were collected simultaneously with the EBSD data, and these spectra were used by the EBSD to assist with the indexing of each pixel; a minimum of 5 bands was required for the display of indexed pixels.

2.3. EPMA mapping

A JEOL JXA 8500F-CL electron probe microanalyzer was used to collect the maps and quantitative point analyses for selected samples. For mapping, wavelength dispersive spectrometry (WDS), energy dispersive spectrometry (EDS), and cathodoluminescence (CL) signals were all collected in parallel (MacRae et al., 2013). The EPMA operating conditions (12 keV; 25 nA; 40 ms dwell; pixel step size and beam defocus both set to 200 nm) were chosen as a compromise to limit beam damage (affecting CL in particular), maximize data collection efficiency, and yet provide CL and X-ray data with adequate signal-to-noise at each pixel to allow for fitting to be utilized. Mapping data were analyzed using the Chimage X *in-house* software (Harrowfield et al., 1993, Torpy et al., 2020). Quantitative data were collected using four WDS spectrometers, with detection limits of around 10 ppm.

2.4. SXRF mapping and μ-XANES measurement

SXRF maps (18.5 keV) and Ge and Cu XANES of the experimental products and natural Zn-Pb ores from the McArthur (HYC) deposits were measured at the X-ray Fluorescence Microscopy (XFM) beamline, the Australian Synchrotron. The polished blocks used for SEM and EPMA characterization were used for the experimental products, and polished ~30 μm-thick sections on quartz slides were used for the HYC Zn-Pb ores samples. The XFM beamline is an undulator beamline with a Si(1 1 1) monochromator (Howard et al., 2020), with an effective energy resolution (ΔE/E) of 2.7×10^{-4} at 10 keV (Liu et al., 2017). Kirkpatrick-Baez mirrors were used to focus the beam to a spot size of ~2 × 2 μm^2. The Maia detector system (Ryan et al., 2010b) was used to collect SXRF maps and XANES data (Ryan et al., 2010a, 2014). The SXRF data were analyzed with GeoPIXE, using the dynamic analysis (DA) method to resolve overlaps and subtract background, escapes peaks and other detector artifacts and produce quantitative elemental images from the full fluorescence spectra (Ryan, 2000; Ryan et al., 2009; Li et al., 2016). Corrections for self-absorption, absorption in air and the efficiency response of the detector were obtained by measuring standard thin metal foils (Ti, Mn, Fe, Cu, Y, Pt) at 18.5 keV and (Ti, Mn, Fe, Cu) at 11.356 keV. These corrections are collectively referred to as the conversion factor. X-ray fluorescence yields are calculated based on a model sample matrix and the conversion factors. The detection limit for Ge depends on the size of the analysis region, pixel dwell and sample matrix, ranging from 2 to 20 ppm in our cases. The uncertainty or error associated with sample concentrations is a root mean squared error of the conversion factor error (typically ~10 %) and uncertainties in the sample matrix thickness (typically 5–10 %) and density variations (typically 10 %).

For Ge XANES, the beam energy was calibrated using GeO_2 and GeS standards; for Cu XANES an in-vacuum Cu metal foil was used to calibrate incident beam energy. XANES data were obtained by collecting SXRF data on 2D-images (maps) or along single horizontal lines (line-XANES method) at 94–101 different monochromator energies spanning the Cu and Ge K-edges (8.979 and 11.103 keV, respectively). The line-XANES method allows for fast data collection by integrating the monochromator movement with the Maia detection system (rather than the x- and y-axes used in 'traditional' XANES imaging using the Maia detector; Etschmann et al., 2010, 2014b). By greatly reducing overheads, the line-XANES method enables collection of XANES data over a few minutes along lines containing 10's or 100's of pixels, suitable for low-concentration samples such as the HYC ores (up to 40 ppm Ge, Spinks et al., 2021). In both cases, individual XANES spectra are constructed by extracting the intensities of the Cu or Ge Kα lines at single pixels at the incident energies visited. Background-subtracted intensities (instead of the raw region of interest counts) were calculated by GeoPIXE; separate DA matrices were used for each beam energy when processing the stack, to track the effects of the changing energy of the Compton and elastic scatter peaks on the background.

As the dwell times on individual pixels are short (0.8–10 ms), it is desirable to average XANES spectra over a range of pixels selected as a function of location, elemental associations, element concentrations, intensity ratios of the Ge/Cu Kα lines at different monochromator energies, or combinations of these different pixel selection methods. This analysis was performed using GeoPIXE

and, in the case of the line-XANES, using *in-house* Matlab code. Note that self-absorption and polarization are not considered in these analyses (e.g., Hens et al., 2019), but are expected to be limited in this case, since Ge concentrations are low (<1 wt% in most cases) and sphalerite is isotropic.

2.5. Ab initio molecular simulations

Geometry optimizations of pure and Ge(IV)/Ge(II)/Fe(II)/Cu(I)-substituted sphalerite were conducted using density functional theory (DFT) within the CPMD code (version 3.17.1, Car and Parrinello, 1985). Similar methods of *ab initio* geometry optimization have been successfully used to calculate the structure of uranyl(VI) complexes in solids (Bühl, 2009); apatite minerals with arsenic substitution (Liu et al., 2017); and uraninite substituted with lead (Syverson et al., 2019). In this study, the BLYP (Becke, Lee, Yang and Parr) exchange correlation-functional was applied (Lee et al., 1988; Becke, 1988) together with Martins–Troullier pseudo-potentials (Troullier and Martins, 1991) with plane-wave cut-offs of 100 Ry.

Geometry optimizations of sphalerite (ZnS) were performed with 8 unit-cells ($2 \times 2 \times 2$ supercell) containing 64 atoms (32 Zn and 32 S) based on the crystal structure of sphalerite from Skinner (1961) (cell length of 10.8186 Å; atomic coordinates in Appendix Table S2). To validate the method and pseudo-potentials of Zn and S, two calculations were conducted with different initial geometries: 1) standard sphalerite structure; and 2) distorted structure to test if the geometry optimization finds the correct crystal structure as listed in Table 2 (Jobs 1–2). The average Zn-Zn, Zn-S, and S-S bond distances of the optimized geometries are within 0.01 Å of the bond lengths from the experimental crystal structure (Skinner 1961; Table S4), even for the simulation that was started with a distorted sphalerite structure. Note that the simulations resulted in slightly distorted Zn-S tetrahedra, with bond lengths varying within ±0.005 Å of the experimental bond length in Job 1, and ±0.019 Å in Job 2. Overall, these tests indicate that the chosen computational method is reliable for optimizing the sphalerite crystal structure. To investigate the effect of vacancies, we conducted simulations with 1 Zn and 1 S removed from the sphalerite structure; this was tested for: 1) 1 Zn and 1 S which were adjacent ($d_{Zn\text{-}S}$ = 2.345 Å) and 2) 1 Zn and 1 S that were further away from each other ($d_{Zn\text{-}S}$ = 7.03 Å) (, Table 2, Jobs 3–4).

The charge balance of Ge(IV) with Zn(II) vacancies was investigated using 8 unit-cells, by replacing two Zn(II) with one Ge(IV) and one vacancy at different relative positions as listed in Table 2, Jobs 5–8. In Job 8, we placed Ge(IV) at very close distances (~0.5 Å) to Zn to test if the geometry optimization can find reasonable crystal structures under extreme scenarios. Four calculations were conducted to characterize the isomorphic substitutions of Zn(II) by Ge(II) and Fe(II), by replacing one Zn(II) with either one Ge(II) (Table 2, Jobs 10–11) or one Fe(II) (Table 2, Jobs 12–13) at different positions. Five calculations were conducted to investigate Ge(IV) uptake via a coupled substitution with Cu(I), by replacing three Zn(II) with two Cu(I) and one Ge(IV) at different positions (Table 2, Jobs 14–18). Finally, five calculations of Fe(II)-Ge(IV) substituted sphalerite were conducted by replacing three Zn(II) with one Fe(II), one Ge(IV) and one vacancy (Table 2, Jobs 19–23). The coordinates of the original Zn and replaced Ge/Cu/Fe and their snapshots are listed in Table S3.

2.6. Thermodynamic modeling

Thermodynamic modeling was conducted using Geochemist's Workbench (Bethke, 2007), with thermodynamic properties for Zn chloride species from Mei et al., (2015), Ge aqueous species from Pokrovski and Schott (1998) and Pokrovski et al. (2005), and Pb chloride species from Etschmann et al., (2018). The standard free energy values of Ge sulfides at 298.15 K and 1 bar are from Pankratz et al., (1987), with updated entropy and heat capacity data from Málek et al., (2011) for GeS_2 and Binnewies and Milke (2008) for GeS. The initial solution compositions (salinity, pH and metal concentrations were chosen to be within the range of typical ore fluid compositions in sedimentary hydrothermal deposits (Wilkinson, 2014).

3. Results

3.1. Germanium distribution and oxidation state in synthesized Zn-Pb ores

3.1.1. Major minerals and textures

The dissolution of calcite and formation of sulfide and sulfate minerals were observed in all experimental runs. Sphalerite (ZnS)

Table 2
List of geometry optimization calculations of sphalerite (ZnS) and Ge(IV)/Ge(II)/Fe/Cu substituted sphalerite.

Job ID	Note	Atoms	initial geometry
1	Standard ZnS	32 Zn, 32 S	standard ZnS
2	Distorted ZnS	32 Zn, 32 S	change x-position of one Zn by 1 Å, closest $d_{Zn\text{-}S}$ = 1.94 Å
3	ZnS vacancy (1)	31 Zn, 31 S	remove 1 Zn and 1 S next to each other (removed d_{ZnS} = 2.34 Å)
4	ZnS vacancy (2)	31 Zn, 31 S	remove Zn and S far from each other (removed d_{ZnS} = 7.03 Å)
5	Ge(IV) substituted ZnS (1)	1 Ge, 30 Zn, 32 S	Ge(IV) at the same position as one of the original Zn (d_{GeS} = 2.34 Å)
6	Ge(IV) substituted ZnS (2)	1 Ge, 30 Zn, 32 S	Ge(IV) placed in between 2 replaced Zn and Ge-Zn/S distances>2.5 Å
7	Ge(IV) substituted ZnS (3)	1 Ge, 30 Zn, 32 S	Ge(IV) placed in between 2 replaced Zn and the closest Ge-S distance at 1.42 Å
8	Ge(IV) substituted ZnS (4)	1 Ge, 30 Zn, 32 S	Ge(IV) placed very close to S at 0.50 Å
10	Ge^{2+} substituted ZnS (1)	1 Ge, 31 Zn, 32 S	Ge^{2+} at the same lattice position as replaced Zn (d_{GeS} = 2.34 Å)
11	Ge^{2+} substituted ZnS (2)	1 Ge, 31 Zn, 32 S	Ge^{2+} at a distorted position at Ge-S distances of 1.94 Å
12	Fe^{2+} substituted ZnS (1)	1 Fe, 31 Zn, 32 S	Fe^{2+} at the same lattice position as replaced Zn (d_{FeS} = 2.34 Å)
13	Fe^{2+} substituted ZnS (2)	1 Fe, 31 Zn, 32 S	Fe^{2+} at a distorted position at Fe-S distances of 1.94 Å
14	Cu^{+} & Ge^{4+} substituted ZnS (1)	2 Cu, 1 Ge, 29 Zn, 32 S	Three replaced Zn aligned as an equilateral triangle; Ge-Cu distance is 3.83 Å
15	Cu^{+} & Ge^{4+} substituted ZnS (2)	2 Cu, 1 Ge, 29 Zn, 32 S	Three replaced Zn aligned as an equilateral triangle; Ge-Cu distance is 6.63 Å
16	Cu^{+} & Ge^{4+} substituted ZnS (3)	2 Cu, 1 Ge, 29 Zn, 32 S	Three replaced Zn aligned as an equilateral triangle; Ge-Cu distance is 7.65 Å
17	Cu^{+} & Ge^{4+} substituted ZnS (4)	2 Cu, 1 Ge, 29 Zn, 32 S	Three replaced Zn aligned in a line, $d_{Ge\text{-}Cu}$ = 3.83/7.65 Å (Ge at the end of the line)
18	Cu^{+} & Ge^{4+} substituted ZnS (5)	2 Cu, 1 Ge, 29 Zn, 32 S	Three replaced Zn aligned in a line, $d_{Ge\text{-}Cu}$ = 3.83 Å (Ge in the middle of the line)
19	Fe^{2+} & Ge^{4+} substituted ZnS (1)	1 Fe, 1 Ge, 29 Zn, 32 S	Three replaced Zn aligned as an equilateral triangle; Ge-Fe distance is 3.83 Å
20	Fe^{2+} & Ge^{4+} substituted ZnS (2)	1 Fe, 1 Ge, 29 Zn, 32 S	Three replaced Zn aligned as an equilateral triangle; Ge-Fe distance is 6.63 Å
21	Fe^{2+} & Ge^{4+} substituted ZnS (3)	1 Fe, 1 Ge, 29 Zn, 32 S	Three replaced Zn aligned as an equilateral triangle; Ge-Fe distance is 7.65 Å
22	Fe^{2+} & Ge^{4+} substituted ZnS (4)	1 Fe, 1 Ge, 29 Zn, 32 S	Three replaced Zn aligned in a line, $d_{Fe\text{-}Ge}$ = 7.65 Å (vacancy in the middle of the line)
23	Fe^{2+} & Ge^{4+} substituted ZnS (5)	1 Fe, 1 Ge, 29 Zn, 32 S	Three replaced Zn aligned in a line, $d_{Fe\text{-}Ge}$ = 3.83 Å (vacancy in the end of the line)

and anhydrite ($CaSO_4$) are the main minerals formed as a result of the dissolution of calcite ($CaCO_3$) and disproportionation of sulfur in Zn-Ge-bearing NaCl solutions (Sample G4 and G2, Fig. 1). The elemental concentrations of the resultant solutions show that most Cu, Fe, Pb and Zn precipitated, and up to 120–1140 mg per litre (mg/L) of Ge remain in the solution, comparable to the Ge oxide solubility in hydrothermal fluids at similar temperature and pH ranges (Pokrovski and Schott, 1998). Globular sphalerite formed around the rim of partially dissolved calcite (Sample G4, Fig. 1A). The clusters contain sphalerite crystals up to 2 μm in size, with some sphalerite globules growing at expense of early-formed anhydrite (Sample G2, Fig. 1B). Iron sulfide crystals were observed with sphalerite clusters and anhydrite in the samples where $FeCl_2$ was added to the initial solution (Sample G8, Fig. 1C). Barite and galena crystals formed together with the sphalerite clusters in experiments containing $PbCl_2$ and $BaCl_2$ (Sample G6 and G9, Fig. 1D-F).

The polished cross-sections show that the new minerals formed a crust around a partially dissolved calcite (Sample G8, Fig. 2A-C). The large gaps between the parent calcite and the newly formed minerals indicate that the dissolution of calcite is more rapid than the precipitation of the new minerals (Fig. 2A, B; Etschmann et al., 2014a; Xia et al., 2009).

EBSD pattern quality and phase maps ascertained the major minerals present in the experimental products (Fig. 3, with typical examples of the indexed diffraction pattern for each phase compiled in Fig. S1). The pattern quality maps (Fig. 3A-D) show the intensity of diffraction patterns (where a whiter pixel implies a better-quality diffraction pattern), indirectly revealing grain boundaries and microstructures within crystals. Phase maps show the identified mineral phases based on indexing the diffraction patterns. EBSD confirms that the crystals rimming the ZnS clusters consist of sphalerite in sample G9 (Fig. 3D, H), and that galena and barite crystals precipitated from solutions containing Pb and Ba (Fig. 3A, E, D, H). Minor covellite (CuS) grains were identified in sample solutions containing CuCl. An example of sample G6 is shown in Fig. 3A, E. The iron sulfide crystals in Sample G8 (Figs. 1C, 2A-C) consist of a mixture of marcasite and pyrite. A few grains of a Ge-rich iron oxide phase were also recognized (Fig. 3G). EDS (collected simultaneously with the EBSD data collection) showed that this phase was predominantly iron oxide with several percent Ge. There was no suitable Ge-Fe-O phase file listed in the crystal structure database used for EBSD phase identification in this study, so an iron oxide phase file was used instead. Although this phase is rare (only a few grains were identified) it is included here for completeness. Sphalerite, anhydrite and the remains of the calcite crystal complete the paragenesis in G8 (Fig. 3B, C, F, G).

3.1.2. Germanium distribution and oxidation state in experimental products

Germanium was observed in sphalerite for all Ge-bearing experiments, determined by the EPMA (samples G8 and G6, Fig. 2C and F) and SXRF microanalysis (Samples G2, G4, G6, G8, G9: Figs. 4–8). The average amount of Ge incorporated into bulk sphalerite is similar for all the samples (0.12–0.24 %, Fig. S2-S5), regardless of the difference in the initial solution composition. In the experiments containing Cu, the Cu-rich phase (covellite) has low Ge concentrations, which could have contributions of the Ge signal from sphalerite below the covellite grain. There are minor individual Ge-rich grains in Sample G8 containing ~10 % Ge (spot 10 in Fig. 2C and Table S1). EBSD identified one of those grains as Ge-bearing iron oxide (Fig. 3G). No significant Ge content was detected in calcite, galena, barite and anhydrite.

SXRF maps of Sample G2 (Fig. 4, GeO_2 and CuCl in the initial solution) show Cu and Ge within the sphalerite clusters, with higher concentrations on the inner edge of sphalerite close to the replaced calcite grains (Fig. 4A). The Ge-Cu correlation plot of the area where the XANES spectra are taken reveals a complex pattern (Fig. S2): (i) A Cu hot spot is poor in Ge (Cu:Ge ≫10) and corresponds to a Cu-sulfide inclusion (Fig. 4C, Fig. S2), possibly covellite as identified by EBSD in other samples (Fig. 3); (ii) There is a general correlation between Cu and Ge in sphalerite, but different trends emerge: the Ge-rich sphalerite rim around the calcite grain shows a correlation between Cu and Ge (Cu:Ge ~3), as does the low Ge-sphalerite that forms the bulk of the replacement (Cu:Ge

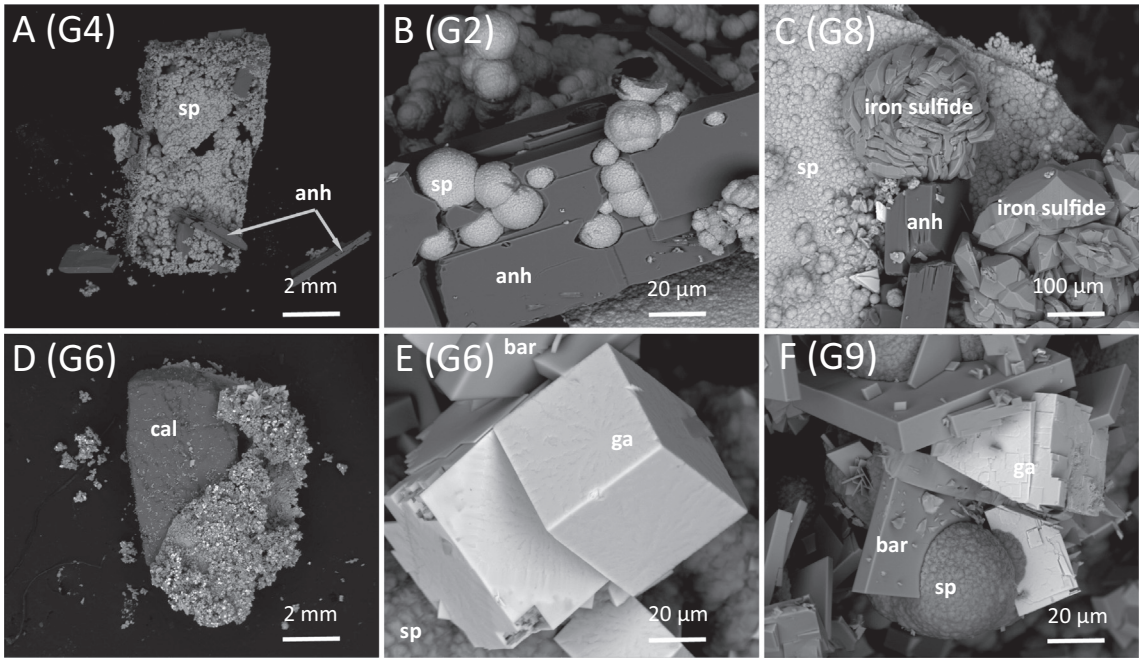

Fig. 1. BSE images of experimental products: A. Sphalerite clusters and anhydrite crystals formed around a dissolved calcite crystal (G4). B. Ge-bearing Sphalerite etching an earlier-formed anhydrite crystal (G2). C. Iron sulfide and anhydrite with sphalerite clusters (G8). D. Sphalerite, galena and barite grains forming a crust on a partially dissolved calcite (G6). E. Cubic galena crystals with barite and sphalerite clusters (G6). F. Inter-growth of galena, barite and sphalerite clusters (G9). sp: sphalerite; ga: galena; anh: anhydrite; bar: barite; cal: calcite.

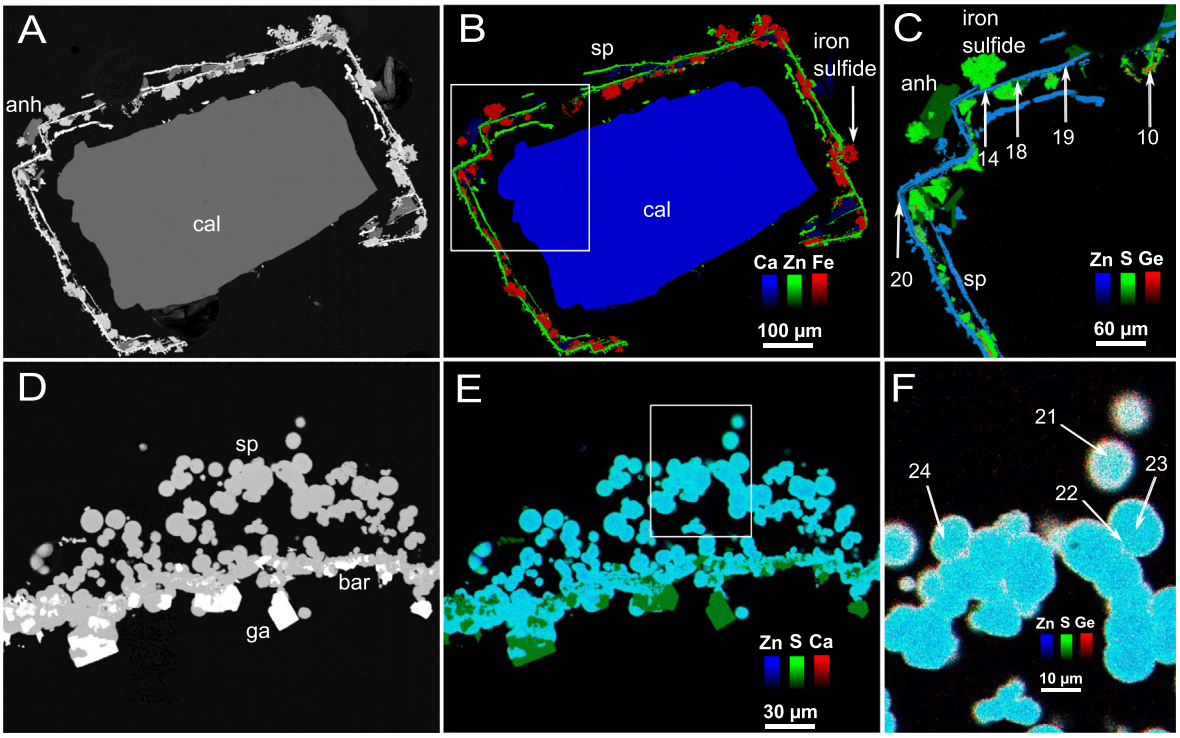

Fig. 2. Back-scattered electron (BSE) images (A, D) and Electron probe microanalysis (EPMA) images (B, C, E, F) of cross-sections for G8 (A-C) and G6 (D-F). Sphalerite, iron sulfide and anhydrite are present in the rim around a partially dissolved calcite sample (G8). Sphalerite clusters, galena and barite formed a crust in sample G6. The locations of Ge quantitative spot analysis are marked in C and F. sp: sphalerite; ga: galena; anh: anhydrite; cal: calcite.

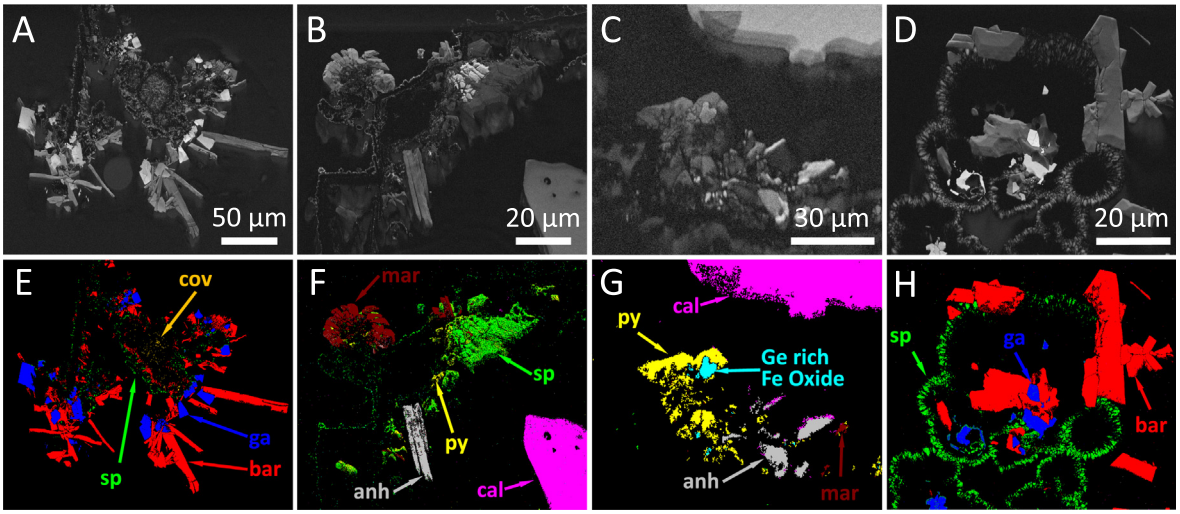

Fig. 3. EBSD Pattern quality maps (A-D, the brightness of the pixels is proportional to the quality of electron diffraction pattern) and phase maps (E-H) of polished cross sections for sample G6 (A, E), G8 (B, C, F, G) and G9 (D, H). sp: sphalerite; ga: galena; anh: anhydrite; bar: barite; cal: calcite; cov: covellite; py: pyrite; mar: marcasite.

~2) (Figs. S1, 4B, 4C). The XANES spectra for the Cu hot spot, Ge hot spots and bulk area are shown in Fig. 4D. There are two points to note: (1) all the spectra are similar to, but broader than the GeS_2 reference spectrum - we refer to this type of XANES spectra as 'GeS_2-type' in the rest of the text; (2) the peaks of the XANES spectra are shifted by ~1 eV towards higher energy relative to the GeS_2 standard. The peak of the XANES from the bulk areas and the Cu-rich spot are shifted to even higher energy (~1.5 eV) compared to XANES from the Ge-rich area. In all cases, however, the edge positions, defined by the maximum in the first derivative of the XANES signal, are identical, and align with the GeS_2 reference (Fig. 4D).

Fig. 5 shows Ge-bearing sphalerite clusters around the rim of a dissolved calcite crystal (Sample G4; $GeBr_2$ and CuCl), with an uneven distribution of Cu (up to 3.4 %, Fig. 5A) and Ge. High Ge contents (up to 0.86 %) are distributed around the edge of the sphalerite clusters, and higher Ge concentrations are again observed on the side closer to the dissolved calcite (Fig. 5A, B). Like G2, the Cu versus Ge correlations reveal different trends with different Cu:Ge ratios ranging from 0.7 to > 10 (Fig. S3). Also note that high Cu and high Ge areas do not overlap (Fig. 5B and C). The Ge K-edge XANES spectra extracted from the spots with high Cu concentration, high Ge concentration, and bulk are identical, i.e., GeS_2-type spectra with a slight (~1 eV) energy shift to higher energy (Fig. 5D).

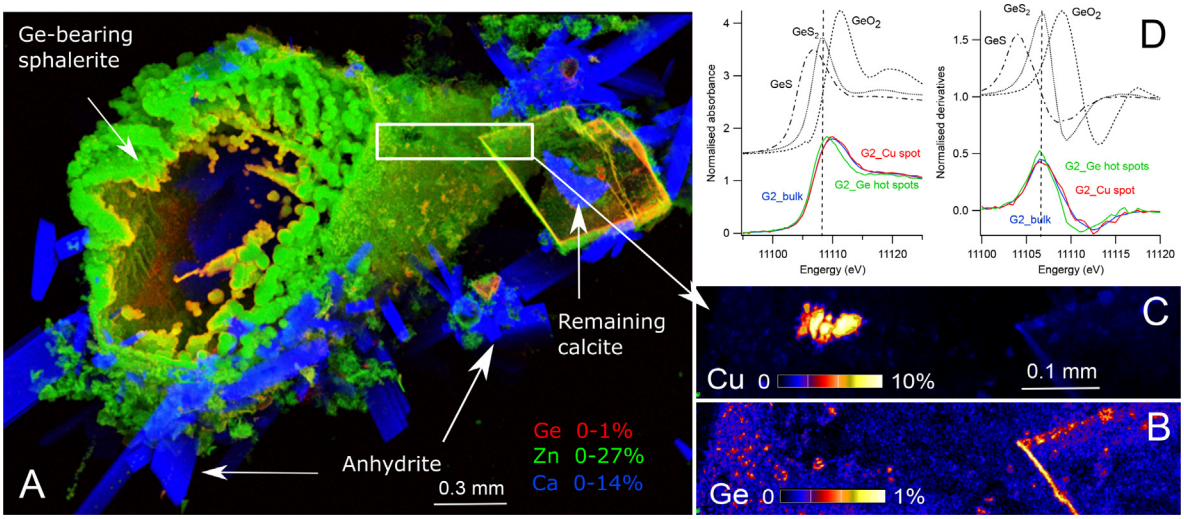

Fig. 4. A. SXRF image of reaction product of sample G2, showing formation of Ge-bearing sphalerite clusters and anhydrite around dissolved calcite crystals. Approximate elemental concentrations (weight percent) of Ge (red), Zn (green) and Ca (blue) are determined by XFM analysis. Individual Ge concentration (B) and Cu concentration (C) are shown for the area where μ-XANES spectra were measured. The μ-XANES spectra and the first derivatives of the high Cu spot, high Ge concentration hot spots, and bulk area are plotted in D, as well as the spectra of Ge(IV) oxide (GeO_2), Ge(IV) sulfide (GeS_2) and Ge(II) sulfide (GeS). (For interpretation of the references to color in this figure legend, the reader is referred to the web version of this article.)

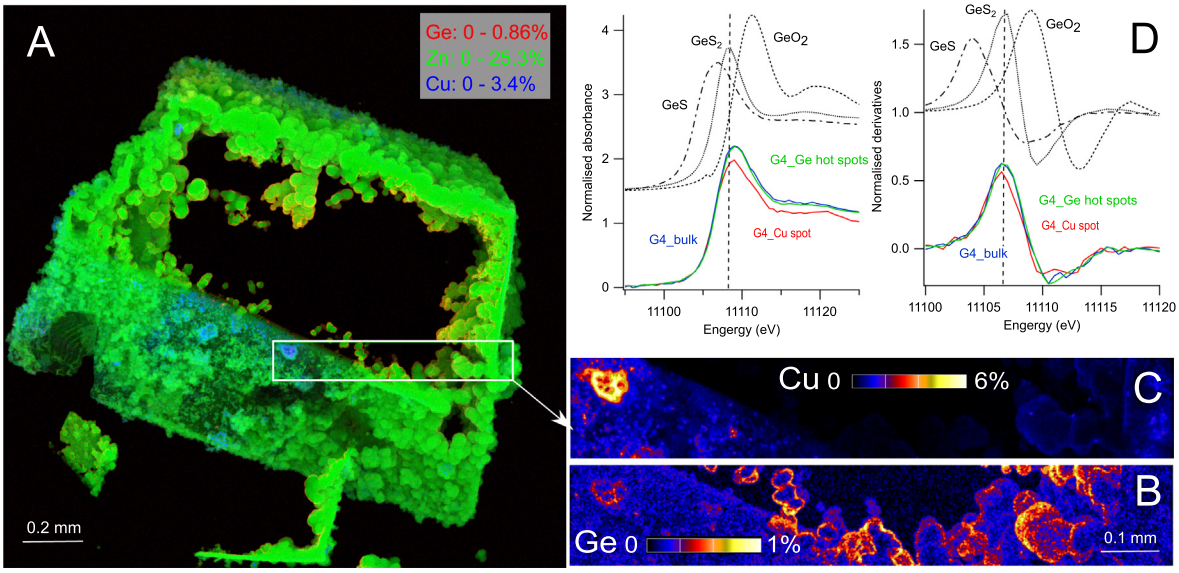

Fig. 5. A. SXRF image of reaction product of sample G4, showing formation of Ge-bearing sphalerite clusters around a dissolved calcite crystal. Approximate elemental concentrations (wt%) of Ge (red), Zn (green) and Cu (blue) in B and C are determined by XFM analysis. Individual Ge concentration (B) and Cu concentration (C) are shown for the area where μ-XANES spectra were measured. The μ-XANES spectra and the first derivatives of the high Cu spot, high Ge hots pots, and bulk area are plotted in D, as well as the spectra of Ge(IV) oxide (GeO_2), Ge(IV) sulfide (GeS_2) and Ge(II) sulfide (GeS). (For interpretation of the references to color in this figure legend, the reader is referred to the web version of this article.)

Similarly, Ge and Cu are unevenly distributed in Sample G6 (with $GeBr_2$, $PbCl_2$, $BaCl_2$, CuCl; Fig. 6). While the Cu hot spots correspond to covellite (Fig. 3E), Ge is distributed in sphalerite, with high Ge around the rim closer to the former calcite grain. Ge concentrations are 0.07–1 % at the rim, and below detection limit in the center of the sphalerite clusters (Fig. 2, Table S1). Again, high Ge and high Cu spots do not overlap. Correlations of Ge-Cu concentrations also show different patterns of Cu:Ge ratios from > 10 to 0.2 (Fig. S4). The Ge XANES spectra collected from both Cu hot spots, bulk areas and Ge hot spots are GeS_2-type spectra with very small (~0.3 eV) peak energy shifting to higher energy (Fig. 6D).

Sample G8 (with $GeBr_2$, $FeCl_2$; Fig. 7) also shows a thin rim of Ge-bearing sphalerite clusters around a partially dissolved calcite crystal (the same crystal shown by EPMA in Fig. 2A-C), with Fe sulfide grains scattered, consistent with the BSE and EPMA images (Figs. 1, 2). The correlations between Fe and Ge concentrations show different patterns. Spots with high Fe-low Ge concentrations have the lowest Ge concentrations, and negative correlations of Fe:Ge (Fig. S5). EPMA results confirm that the iron sulfides (pyrite and marcasite identified by EBSD) do not contain appreciable Ge. The bulk area of sphalerite has an average Fe:Ge ratio of ~6, while Ge hot spots have a Fe:Ge ratio of ~3 (Fig. S5). Germanium associated with the bulk sphalerite and high Fe-low Ge spots has GeS_2-type

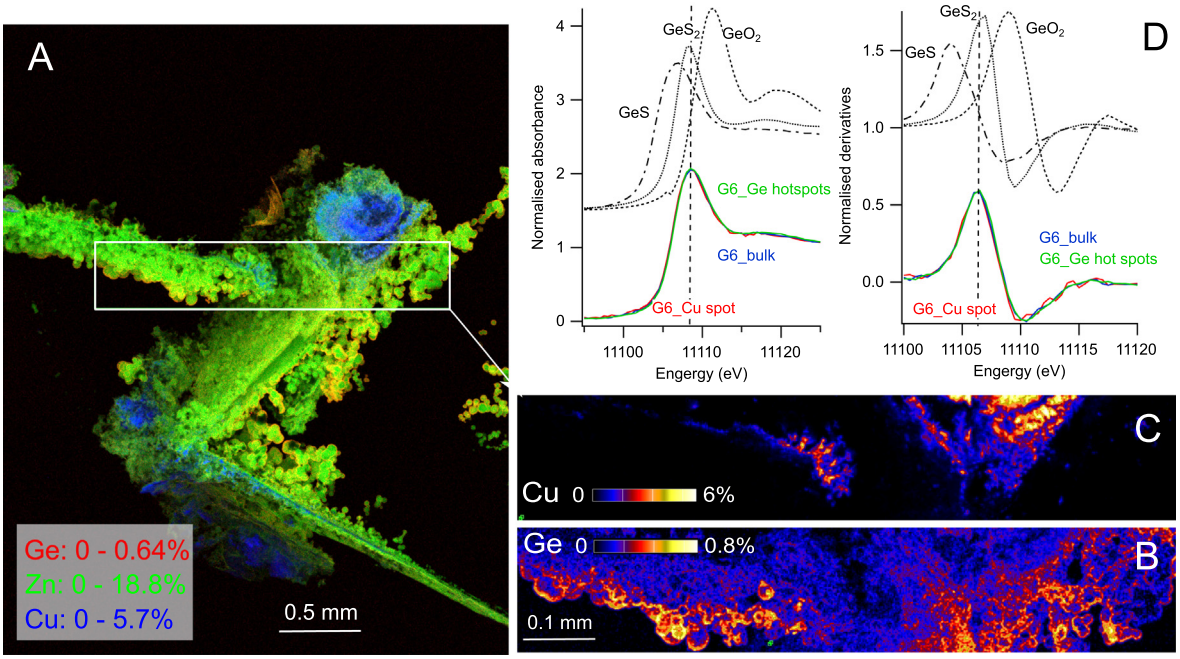

Fig. 6. A SXRF image of reaction product of sample G6. B. The area where micro-XANES spectra were measured, showing high concentration Ge around the rim of sphalerite clusters. Approximate elemental concentration (wt%) of Ge (red), Zn (green) and Cu (blue) in B and C are determined by XFM analysis. Individual Ge concentration (B) and Cu concentration (C) are shown for the area where micro-XANES spectra were measured. The μ-XANES spectra and the first derivatives of the high Ge hot spots, a Cu hot spot and bulk area are plotted in D, as well as the spectra of Ge(IV) oxide (GeO_2), Ge(IV) sulfide (GeS_2) and Ge(II) sulfide (GeS). (For interpretation of the references to color in this figure legend, the reader is referred to the web version of this article.)

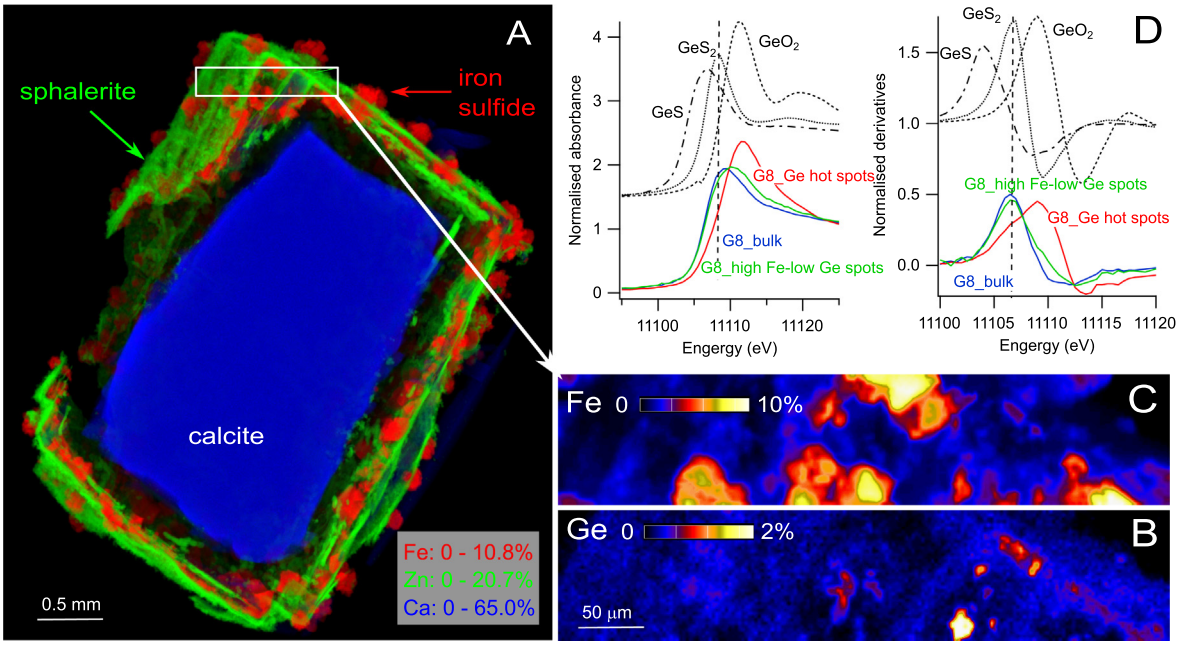

Fig. 7. (A). SXRF image of reaction product of sample G8. Approximate elemental concentrations (wt%) of Fe (red), Zn (green) and Ca (blue) are determined by XFM analysis. (B) and (C) are the area shown in the box in (A) where μ-XANES imaging were measured, showing Fe (B) and Ge concentration (C). (D) shows count rate association of Fe and Ge in the box. (E) and (F) show μ-XANES spectra (E) and the first derivatives (F) of Ge hot spots (Ge rich Fe oxide inclusions, high Fe-low Ge spots and bulk area (the rest of the area), as well as spectra of Ge(IV) oxide (GeO_2), Ge(IV) sulfide (GeS_2) and Ge(II) sulfide (GeS). (For interpretation of the references to color in this figure legend, the reader is referred to the web version of this article.)

spectral feature with the peak shifting to higher energy by ~1 and ~1.5 eV, respectively (Fig. 7D). The Ge hot spots are inclusions of Ge-rich Fe oxide, and their XANES spectra differ markedly from the GeS_2-type: they show an edge position identical to the Ge(IV) oxide reference, but with a broader white line (Fig. 7D). This is consistent of the EBSD results of a Ge-rich Fe oxide grain (Fig. 3G).

Finally, sample G9 (with $GeBr_2$ but no Fe, no Cu) has Ge evenly distributed in the bulk area of sphalerite clusters, except for a few

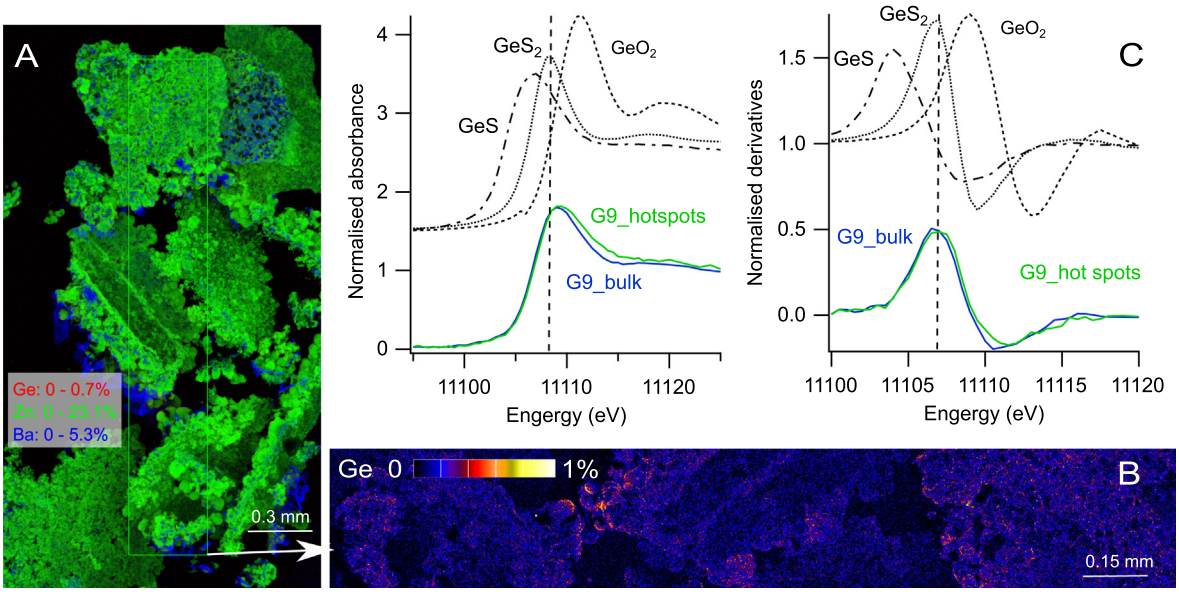

Fig. 8. A. SXRF image of reaction product of sample G9 (no Fe or Cu added). Approximate elemental concentration (wt%) of Ge (red), Zn (green) and Ba (blue) in B and C are determined by XFM analysis. B. The area where μ-XANES spectra were measured, showing relatively high concentration Ge (up to 1%) around the rim of sphalerite clusters. The μ-XANES spectra and the first derivatives of high Ge concentration hotspots (Green areas in the inset of C) and bulk area (the area that is not green), as well as the spectra of Ge(IV) oxide (GeO_2), Ge(IV) sulfide (GeS_2) and Ge(II) sulfide (GeS). (For interpretation of the references to color in this figure legend, the reader is referred to the web version of this article.)

hot spots (Fig. 8). All spectra collected from the bulk area and hot spots are similar with GeS_2-type spectral feature and peak energy shifts of ~1 eV (Fig. 8C).

When plotting the XANES spectra for all the samples together (Fig. 9A), one can see the GeS_2-type spectra predominate, with varying degrees of edge shift towards higher energy, reflecting contaminations of Ge(IV) oxide component; however, the contamination is minimal, judging by the identical edge positions of the derivatives (Fig. 9b). The spectra of sample G2 have largest edge shift, due to the starting source being GeO_2 instead of $GeBr_2$ as in the others.

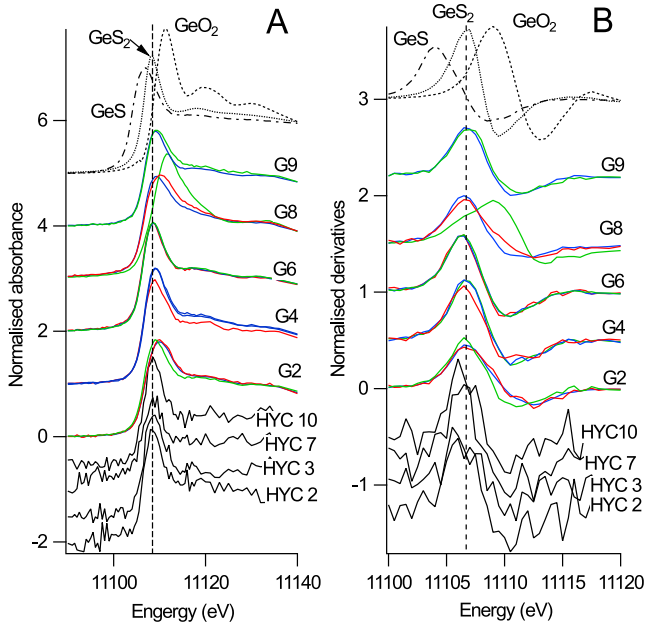

Fig. 9. Germanium K-edge XANES spectra (A) and the first derivatives (B) for HYC sphalerite (HYC2, 3, 7, 10), synthetic Ge-bearing sphalerite (G2, 4, 6, 8, 9, blue line color: bulk area; red and green: hot spots. See Figs. 4–8) and Ge compounds (GeS, GeS_2 and GeO_2). (For interpretation of the references to color in this figure legend, the reader is referred to the web version of this article.)

3.2. Germanium distribution and oxidation state in HYC Zn-Pb ores

Germanium K-edge XANES spectra were collected for ores from the McArthur River (HYC) sediment-hosted Zn-Pb-Ag deposit in the Carpentaria Zn belt, northern Australia. High-grade HYC ores (>10 wt% Zn) generally contain 10–40 ppm Ge (Spinks et al., 2021). The SXRF images (Fig. 10) highlight the finely laminated nature of the ores as well as features of carbonate dissolution and replacement by sphalerite. A detailed discussion of ore microtextures, geology, and the formation of the HYC deposit is provided by Spinks et al. (2021).

The Ge XANES spectra collected from the HYC ores are very similar to each other and have GeS_2-type spectra features like the experimental spectra, though much noisier than the latter due to low concentrations of Ge in sphalerite (up to 40 ppm). The peak positions are identical to that of the GeS_2 reference, i.e., no edge shift (Fig. 9), indicating an oxidation state of Ge(IV) bonded with sulfur in these samples.

3.3. Copper speciation in synthesized sphalerite

Copper K-edge XANES spectra were collected at different spots within sphalerite clusters from an experimental sample (sample G6, same area as the Ge). All the Cu XANES spectra from experimental sphalerite are identical, and identical to the spectra collected for Cu in the lattice of natural sphalerite (Cook et al., 2012; Belissont et al., 2016). When compared to XANES spectra of common Cu sulfide minerals, Cu-in-sphalerite closely resembles chalcopyrite (Fig. 11). This is due to the similar coordination environment of Cu in chalcopyrite and when it replaces Zn in ZnS; in either case, Cu is tetrahedrally coordinated to four sulfur atoms (Vaughan & Corkhill, 2017).

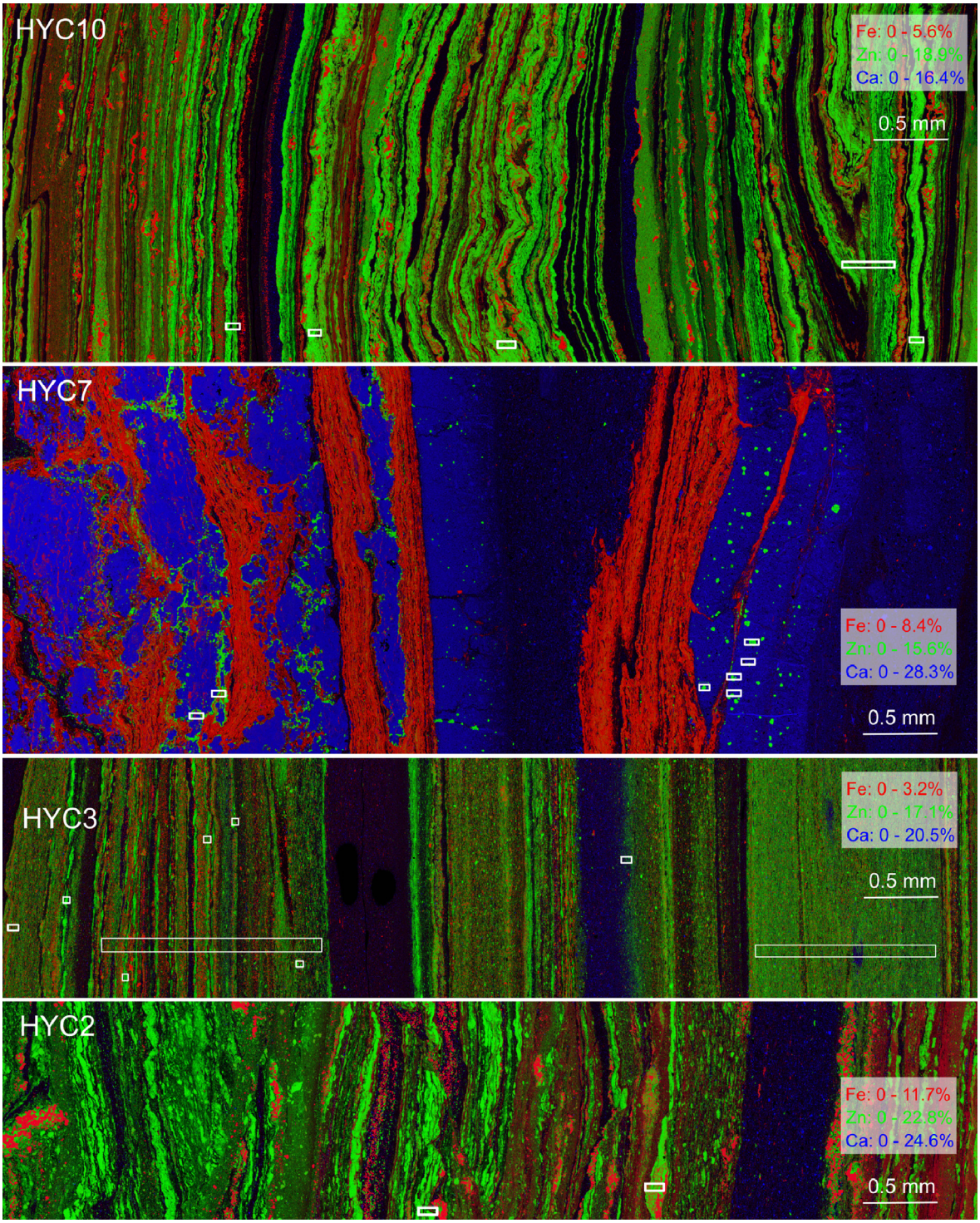

Fig. 10. SXRF images of the thin sections of ore samples from the HYC Zn-Pb deposit. Red: Fe, Green: Zn, Blue: C. The boxes show the positions of the Ge K-edge XANES measurement along the bottom line of each box. (For interpretation of the references to color in this figure legend, the reader is referred to the web version of this article.)

3.4. Results from ab initio molecular simulations

3.4.1. Geometry optimization of vacancy-bearing sphalerite

In jobs 1 and 2 (pure sphalerite), distances in individual Zn-S tetrahedra were found to vary slightly (< ±0.02 Å) relative to the symmetry-constrained experimental distance of 2.342 Å (Skinner, 1961; Table S4). When vacancies were introduced by removing an adjacent Zn-S pair (Job 3) or removing a Zn and a distant S (Job 4; Fig. 12), the structure relaxed more, with individual Zn-S bonds within ±0.111 Å of the experimental bond lengths, but again the averaged bond lengths were 2.35 and 2.36 Å, respectively, close to the experimental bond lengths.

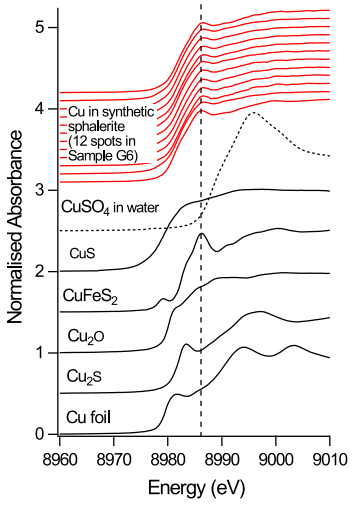

Fig. 11. Cu K-edge XANES spectra of Cu compounds and synthetic sphalerite sample G6.

Indeed, in all the subsequent optimizations, regardless of the substitution, the Zn-S, Zn-Zn, S-S bond lengths averaged over the 8 units cells were close to that in the experimental sphalerite structure (Tables S5-S10), with the Ge-S distance stabilizing after 1000–2000 optimization steps (Figs. S5-S8).

3.4.2. Geometry optimization of Ge(IV) charge balanced by vacancy

Substituting one Ge(IV) into the 8-unit cell structure of sphalerite results in an effective concentration of ~2.4 wt%. Ge(IV) was introduced into the sphalerite lattice (a) substituting on a Zn site and removing a distant Zn (Job 5); (b) removing two adjacent Zn and placing the Ge(IV) between them (Job6); (c) replacing two Zn with one Ge(IV) located such that the closest Ge-S distance was 1.42 Å (Job7); (d-e) replacing two Zn with Ge(IV) such that the Ge (IV) was placed very close to a S (~0.5 Å, Job 8) (Fig. 13).

In these simulations, Ge is assumed a coordination varying from 3-fold to 5-fold, with Ge-S bond lengths ranging from 2.05 to 2.53 Å, but most bond lengths were around 2.2 Å. The change of Ge-S distance reflects the small ionic size of Ge(IV) compared to Zn(II) (0.39 Å vs 0.6 Å, Shannon, 1976). The Zn-S bond lengths close

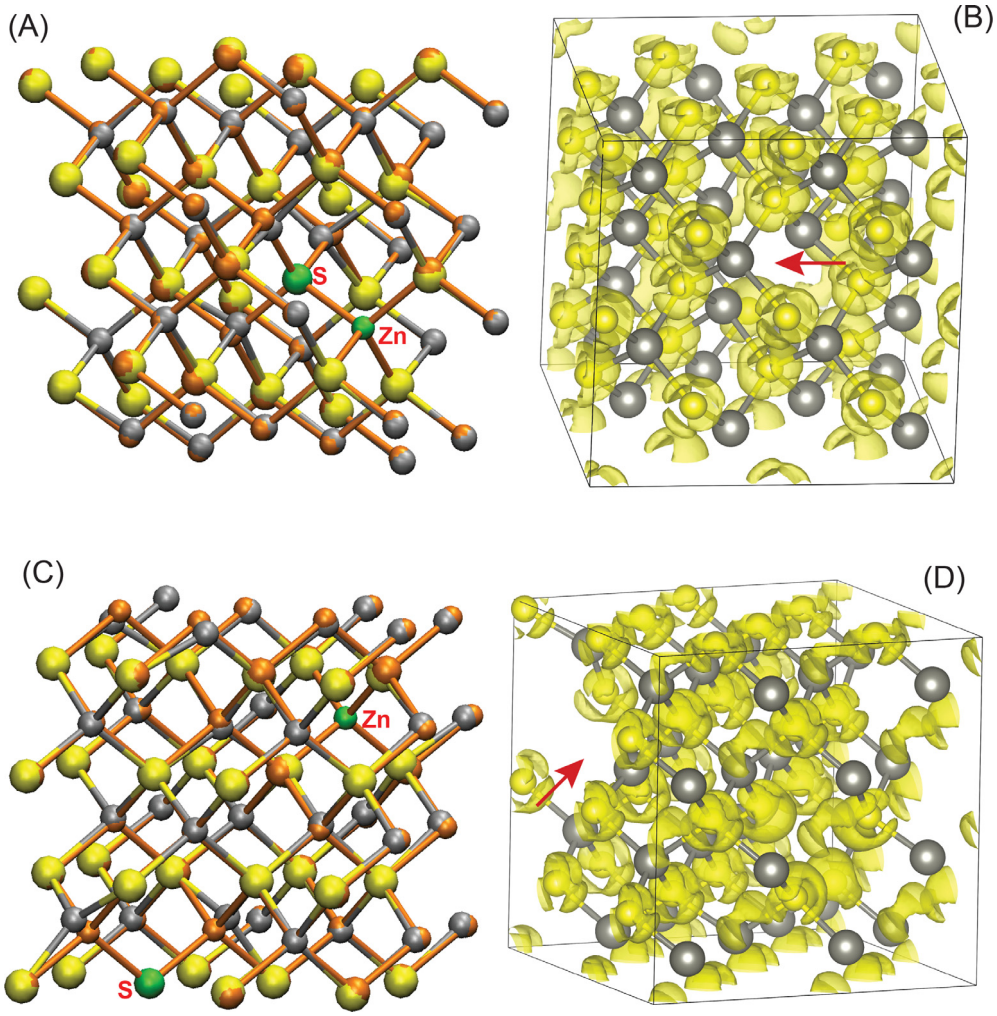

Fig. 12. (a, c) original sphalerite structure and optimized geometry of sphalerite with vacancy for Jobs 3 and 4. (b, d) Electron density of optimized sphalerite with vacancy for jobs 3 and 4. (orange ball and sticks = original sphalerite structure; green ball = highlight the removed Zn and S; grey ball = optimized Zn position; yellow ball = optimized S position; yellow clouds = electron density with isosurface level at 0.835; red arrow shows the vacancy). (For interpretation of the references to color in this figure legend, the reader is referred to the web version of this article.)

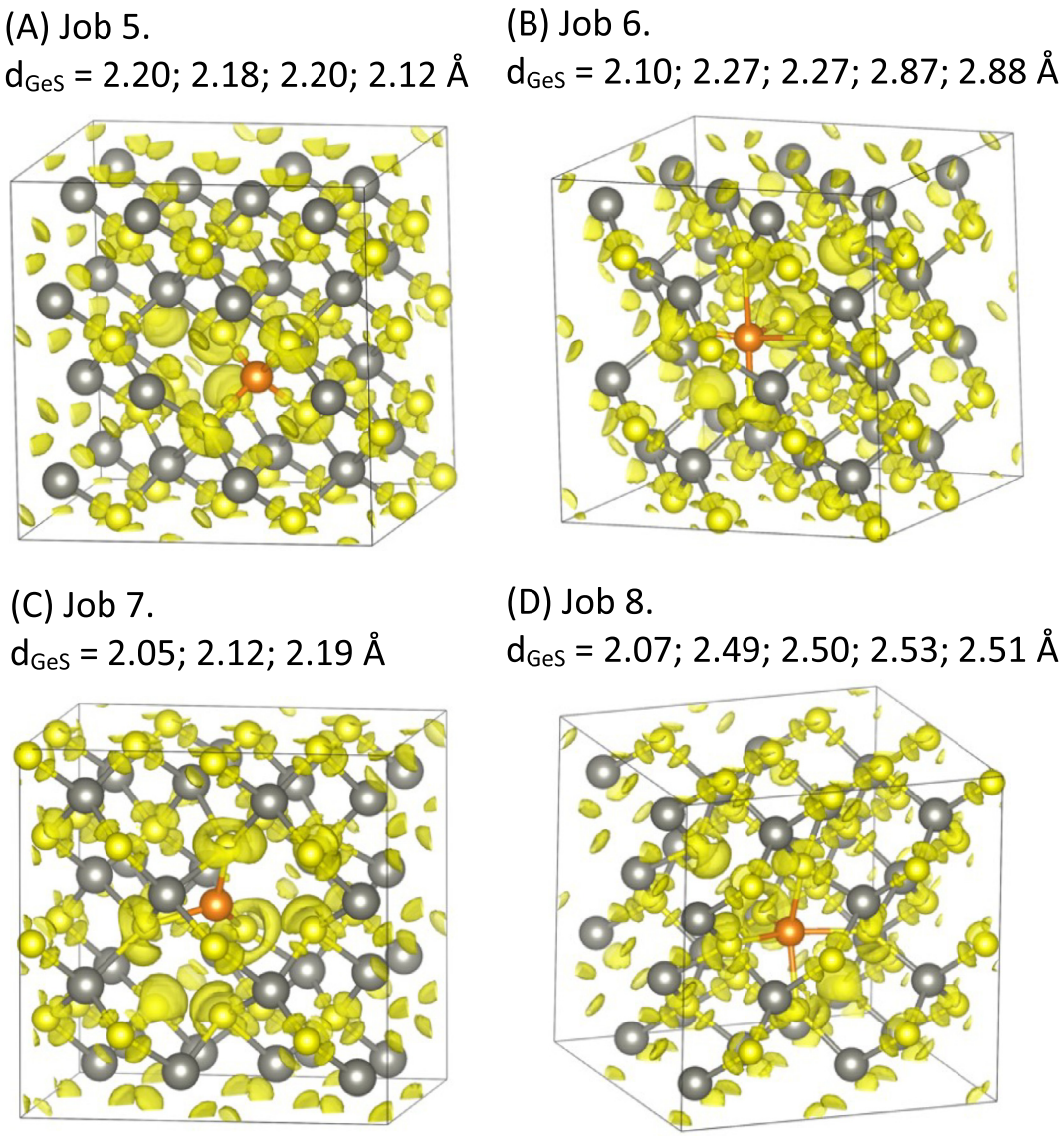

Fig. 13. Snapshots of optimized geometry for Ge incorporation in sphalerite via the $2Zn^{2+} = Ge^{4+} + \square$ coupled substitution (Jobs 5–8). Grey ball = Zn; yellow ball = S; orange ball = Ge; yellow clouds = electron density with isosurface level at 0.865. (For interpretation of the references to color in this figure legend, the reader is referred to the web version of this article.)

to the Ge(IV)/vacancy sites vary significantly from the equilibrium distance (up to ± 0.33 Å), while Zn further away are close to the original Zn-S bond lengths. The electron density plots further highlight the geometry distortion: bonds that are shorter than the average Zn-S = 2.342 Å have electron density 'pushed' to the far side of the sulfur, i.e., further away, while longer bonds and areas around vacancies enable excess charge to 'pile up'.

3.4.3. Geometry optimization of Ge(II)- or Fe(II)-substituted sphalerite

Geometry optimizations of Ge(II)- or Fe(II)-substituted sphalerite were conducted by (a) substituting the divalent ion onto a Zn site and (b) at a distorted position such that the initial Ge/Fe-S distances were 1.94 Å (Fig. 14A, B).

In either case, the Ge(II)-substituted into sphalerite maintained a distorted tetrahedral geometry with Ge(II)-S bonds ranging from 2.438 to 2.495 Å. Fig. 14A shows significant asymmetry in the electron density around Ge(II); this is consistent with an electron lone pair typical of Ge(II) (Holloway and Melnik, 2001), although the lone pair resulted in only a slight distortion of the Ge(II) coordination. The longer Ge(II)-S bonds compared to the Ge(IV)-bonds could be attributed to the larger ionic radius of Ge(II) ~0.73 Å (Shannon, 1976). The surrounding ZnS bonds accommodated the Ge(II) with varying bond lengths, ranging from 2.302 to 2.379 Å.

Similarly, substituting Fe(II) into sphalerite results in some distortion in the nearby ZnS bonds (bonds ranging from 2.286 to 2.411 Å, with an average Zn-S distance of 2.35 Å). The Fe(II)-S bonds ranged from 2.251 to 2.323 Å, slightly shorter than the average Zn-S bonds, despite similar ionic radii of Fe(II) (0.63 Å) and Zn (II) (0.60 Å). Overall, the local distortions induced in the sphalerite structure by substitution of Ge(II) or Fe(II) are less than when Ge (IV) was substituted (Table S6, Table S7).

3.4.4. Geometry optimization of Cu(I) and Ge(IV)-substituted sphalerite

Geometry optimizations of Cu(I) and Ge(IV)-substituted sphalerite (Jobs 14–18; Fig. 14C,D) were calculated by replacing three Zn(II) with two Cu(I) and one Ge(IV) at five different configurations. For all five calculations, the optimized geometry of the Cu (I) and Ge(IV) maintained a distorted tetrahedral structure. The Ge-S distances ranged from 2.169 to 2.247 Å, the Cu-S distances

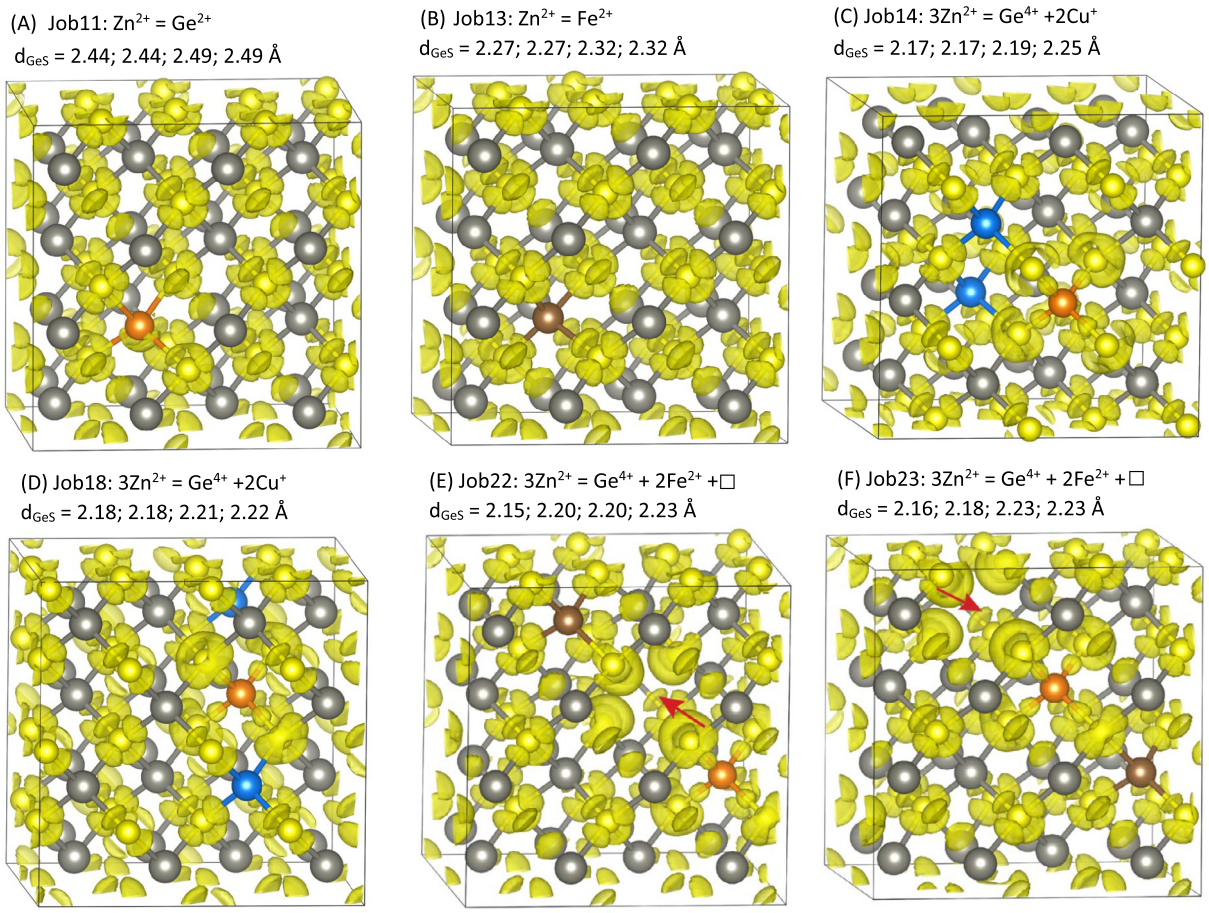

Fig. 14. Snapshots of optimized geometry for Ge incorporation in sphalerite via the Zn^{2+} = Ge^{2+} (A) compared to Fe^{2+} substitution (B); Ge(IV) incorporation via the coupled substitution $3Zn^{2+}$ = Ge^{4+} + $2Cu^{+}$ (C, D); and co-substitution of Zn(IV) and Fe(II) following the $3Zn^{2+}$ = Ge^{4+} + □ + Fe coupled substitution (E, F) (□ refers to vacancy). Grey ball = Zn; yellow ball = S; orange ball = Ge; brown ball = Fe; blue ball = Cu; yellow clouds = electron density with isosurface level at 0.85. Red arrows in E, F points the vacancies. (For interpretation of the references to color in this figure legend, the reader is referred to the web version of this article.)

ranged from 2.255 to 2.385 Å, and the Zn-S distances varied from 2.242 to 2.540 Å (Table S8).

Compared to the optimized geometry of one Ge(IV) + a vacancy replacing two Zn(II) in sphalerite (Jobs 5–8), which resulted in Ge-S distances of 2.050 – 2.530 Å, Jobs 14–18 highlight a more rigid Ge (IV)-S distance of 2.169–2.247 Å. This is likely due to the absence of vacancy in the crystal structure as two tetrahedrally-coordinated Cu(I) occupy the original Zn position. Compared to Ge(II)-substituted sphalerite (Jobs 11–12), Ge(IV)-S distances (2.19–2.21 Å) are shorter than Ge(II)-S distances (2.46 Å).

3.4.5. Geometry optimization of Fe(II) and Ge(IV) substituted sphalerite

The geometry optimizations for sphalerite where three Zn(II) were replaced with one Fe(II), one Ge(IV) and one vacancy were conducted in Jobs 19–23. Like Jobs 14–18, the results show that the substituted atoms maintain a distorted tetrahedral structure with the nearby sulfur atoms (Fig. 14E, F), with Ge-S distances of 2.148–2.233 Å, Fe-S distances of 2.197–2.361 Å, and Zn-S distances 2.233–2.547 Å (Table S9).

4. Discussions

4.1. Ge oxidation state in sphalerite

The μ-XANES data show that Ge exists as Ge(IV) in sphalerite for all the experiments, and the spectral features are broadly similar (Figs. S2-S5) regardless of whether the starting material was Ge (II) bromide ($GeBr_2$) or Ge(IV) oxide (GeO_2). The μ-XANES data collected from the HYC Zn ores also show a Ge(IV) oxidation state. Several previous studies used synchrotron μ-XANES to investigate the oxidation state of Ge in natural sphalerite. Cook et al. (2015) observed Ge(IV) in Ge-bearing sphalerite from the carbonate-hosted Mississippi Valley-Type Tres Marias Zn deposit, Mexico (Saini-Eidukat et al., 2009); they show that Ge in this sphalerite produced XANES spectra like GeS_2 glass, germanite, renierite and argyrodite. Similarly, Belissont et al. (2016) observed Ge(IV) in Ge-bearing sphalerite from the vein-type Saint-Salvy deposit, France. Therefore, our experimental results and the data from most studies on natural sphalerite confirm the predominance of Ge(IV) under hydrothermal conditions near the sulfate/sulfide boundary as in sediment-hosted Zn-Pb deposits. This is also consistent with the Ge(IV) spectra collected in hydrothermal chalcopyrite (Belissont et al., 2019; Etschmann et al., 2017), and coal and roll-front deposits (Etschmann et al., 2017). These studies are consistent with the experimental studies showing that aqueous Ge(IV) predominate in typical hydrothermal fluids (Pokrovski and Schott, 1998; Pokrovski et al., 2005). In contrast, Bonnet et al. (2017) found convincing XANES evidence of the presence of both Ge(II) and Ge(IV) in sphalerite from Mississippi Valley-Type deposits, Tennessee, USA. As highlighted by Bonnet et al. (2017) and illustrated in the logfO_2(g) vs pH diagrams in Fig. 15, Ge(II) is not stable in water. Even in highly reducing environments such as coal, Ge(IV) predominates (Etschmann et al., 2017). Indeed, Bonnet et al.

(2017) is the only study to date to provide direct evidence for Ge(II) in natural rock. Experimental and empirical fractionation data suggest that Ge(II) is only likely important in highly reduced and dry lunar basalts (Dickinson et al., 1989; Mare et al., 2020). Hence the likely presence of Ge(II) in the overall oxidized (pyrite, barite) carbonate-hosted Tennessee deposits remain enigmatic.

The measured Cu K-edge XANES of experimental sphalerite resemble that of chalcopyrite (Fig. 11), indicating that the oxidation state of Cu is Cu(I). These results are also consistent with Cu (I) oxidation state determined in natural sphalerite by Cook et al. (2012, 2015), Belissont et al. (2016), and Filimonova et al. (2019).

Liu et al. (2021) attribute the formation of very fine sphalerite crystals with a poor diffraction pattern in the center of sphalerite globules to rapid nucleation during the initial stages of the fluid reacting with H_2S; larger crystals formed around the rims of sphalerite globules suggest a slowing down of the growth rate as the reaction progresses and Zn becomes depleted in solution. Similarly, we speculate that the Ge in the bulk of the sphalerite clusters occurred in the early stage of rapid sphalerite precipitation, and the high concentrations (hot spots) of Ge around the rims of sphalerite clusters are caused by the slow precipitation of large sphalerite crystals with more time for Ge substitution, which also explains high Ge concentrations in the sphalerite near the remaining calcite.

4.2. Ge substitution mechanism

Our experiments show that, among the major minerals formed in the experiment, Ge preferentially partitions to sphalerite rather than galena, other Cu-Fe-sulfides (e.g., pyrite, marcasite and covellite) and sulfate minerals (anhydrite and barite). Our experimental results confirmed the observed behavior of trace element partitioning in co-existing Zn-Cu-Pb sulfides in natural samples, i.e., Ge preferentially partitions into sphalerite (e.g., Cook et al., 2009, Ye et al., 2011).

Trace element incorporation into sphalerite is intrinsically controlled by the nature of the chemical bond, the similarity in the size of the lattice site and charge balance (e.g., Johan, 1988; Belissont et al., 2014, Goldmann et al., 2019). The incorporation is also affected by the concentration and speciation of the involved elements in aqueous fluids, as well as formation temperatures and pressures (e.g., Belissont et al., 2016). Previous studies have proposed various mechanisms of Ge(IV) substitution in sphalerite, with charge balance achieved by the incorporation of di- and monovalent elements such as Cu(I) and Cu(II), based on the correlation between the concentrations of Ge and other elements in sphalerite, or absence of such correlations:

$$2\mathrm{Cu(I)} + \mathrm{Cu(II)} + \mathrm{Ge(IV)} = 4\mathrm{Zn(II)}\ (\quad) \tag{2}$$

$$2\mathrm{Zn(II)} = \mathrm{Ge(IV)} + \mathrm{vacancy}\ (,\ ) \tag{3}$$

$$3\mathrm{Zn(II)} = \mathrm{Ge(IV)} + 2\mathrm{Cu(I)}\ (\quad) \tag{4}$$

Cook et al. (2015) concluded that vacancies are the main mechanism of Ge incorporation in their sphalerite from the Tres Marias Zn deposit, Mexico, and Goldmann et al.'s (2019) nanometer-scale study on Ge-rich sphalerite from Tres Marias show that Ge is indeed homogeneously incorporated into the sphalerite lattice. Belissont et al. (2016) proposed that Ge(IV) substitution can proceed through the charge balance of other elements (e.g., Cu(I)) or vacancies. They suggested that vacancies would enable the Ge (IV) for Zn(II) substitution, further enhanced by the Fe content in sphalerite, despite the fact that the substitution of Ge(IV) for Zn(II) is unlikely according to the Goldschmidt rule because the difference between the ionic radii of Ge(IV) (0.39 Å) and Zn(II) (0.6 Å, Shannon, 1976) is >15 %. Also, Fe(II) has the same charge as Zn(II), therefore is not expected to influence the Ge(IV) substitution in sphalerite for charge balance reason. Note that high Germanium is also found in Fe-poor sphalerite from the Red Dog deposit, Alaska (Kelly et al., 2004). A recent study (Li et al., 2020) proposed a Ge substitution equation including multiple trace elements (Cu, Sb, Ag) to explain the trace element correlation in sphalerite from the Maozu Pb-Zn deposit, China. All these studies highlight the diverse ways Ge can be incorporated into sphalerite.

Our experimental data show that a similar amount of Ge can be readily substituted into sphalerite, with or without Cu(I) for charge balance. For the Cu-bearing samples, Ge substitution occurred in all the sphalerite with variable Cu/Ge ratios, indicating multiple ways (vacancies and other cations) to achieve charge balance in Ge incorporation in sphalerite. The MD simulation results demonstrated that the average Zn-S, Zn-Zn and S-S bond lengths were close to those in the experimental sphalerite structure for all simulations with Ge substitutions, able to accommodate high levels ($\geq$3 mol%) of Ge with and without coupled replacement with other cations. This illustrates the resilience and flexibility of the sphalerite crystal structure. The MD simulations also showed that Ge (II) can be substituted into sphalerite. Therefore, the observed Ge (IV) in our experimental and natural sphalerite of the HYC deposits and other Zn deposits (Cook et al, 2015, Belissont et al., 2016) is likely to be determined by the oxidation state of Ge(IV) in fluids.

Our experimental and MD results explain the complex and diverse Ge incorporation scenarios observed in nature as mentioned in the previous paragraph, implying that the correlation between Ge and other trace elements in natural sphalerite may not necessarily result from coupled substitutions. These elements may simply precipitate simultaneously from the same hydrothermal fluids. This could be the case when a positive correlation of Ge with multiple trace elements is observed (e.g., the multiple-trace elemental correlation observed by Li et al., 2020).

4.3. Behavior of Ge in hydrothermal Zn ore formation

We conducted thermodynamic modeling of a metal-bearing brine reacting with reduced sulfur and carbonate at 200 °C and water vapor-saturated pressure, to assess the behavior of Ge under hydrothermal conditions such as sediment-hosted Zn deposits. At present, it is premature to calculate the aqueous Ge solubility of Ge-bearing sphalerite, as a thermodynamic model and properties for Ge(IV) incorporation in sphalerite (like As in pyrite, e.g., Xing et al., 2019) are lacking. Therefore, modeling for Ge is only to approximate the stability and oxidation state of aqueous Ge species vs Ge sulfide minerals (i.e., Ge oxides are not included).

The modeling results (Fig. 15A) show that the predominant Ge species in acidic-neutral hydrothermal brines are $Ge(OH)_4(aq)$, the main Ge species in hydrothermal fluids proposed by Pokrovski and Schott (1998) and Pokrovski et al., (2005). GeS_2 is stable in acidic-neutral fluids under reduced conditions, with a small stability field of GeS under extremely reduced conditions (Fig. 15A). A Zn, Pb and Ba-bearing brine reacting with reduced sulfur and carbonate would precipitate most of the metals from the solution: from point 1 to point 2, 93 % of Ba, 97 % of Pb and 99.99 % of Zn precipitated from the fluid after reacting with H_2S and carbonate (Fig. 15B, Table S10). Notably, the final pH and $\log fO_2$ of the reaction path are within the field of GeS_2, consistent with the Ge(IV) XANES spectra measured from the experimental and natural Ge-bearing sphalerite. Further studies are needed to obtain the thermodynamic properties of Ge(IV) substitution in sphalerite before we can quantify the aqueous Ge solubility of Ge-bearing sphalerite.

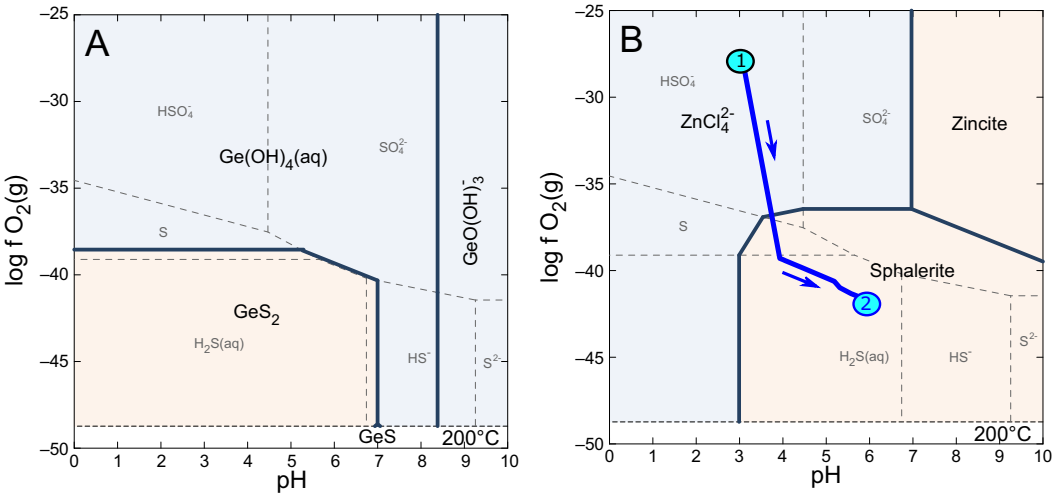

Fig. 15. LogfO_2(g) - pH diagrams of predominant Ge species (A) and Zn species (B) at 200 °C and water vapor-saturated pressure (∑S = 0.2 m, NaCl = 3 m, Zn = 0.1 m, Ge = 0.1 m). The change of pH and logfO_2(g) of a reaction path modeling (Point 1 to Point 2) is plotted in B. The reaction path is result of mixing a Zn-Pb-Ba-bearing, sulfur-poor brine with 0.2 m H_2S(aq), with the presence of calcite at water vapor-saturated pressure and 200 °C (The initial and final Zn, Pb and Ba compositions of the fluid see Table S10).

5. Conclusions

1. Hydrothermal experiments have been successfully conducted to synthesize Ge-doped Zn-Pb ores at 200 °C and water vapor-saturated pressure.
2. Micro-characterization of experimental products shows that Ge (IV) is incorporated into sphalerite with and without added Cu (I) and Fe(II) chloride in the initial solutions, regardless of the Ge source being Ge(II) bromide or Ge(IV) oxide. Copper exists as Cu(I) in the experimental sphalerite.
3. Ge(IV) with XANES spectra similar to the experimental sphalerite is also observed in natural zinc ore samples from the MacArthur River Zn-Pb-Ag deposits, Australia.
4. *Ab initio* quantum chemical simulations confirm that sphalerite can readily accommodate Ge via charge balance by vacancies and by coupled substitutions, with the crystal structure and average Zn-S, Zn-Zn, S-S distances retained when replacing > 3 mol% of the Zn sites with Ge(IV), Ge(II), Cu(I) or Fe(II).
5. In summary, we show that Ge(IV) can be substituted in hydrothermal sphalerite under conditions like the sediment-hosted Zn-Pb deposits. Germanium substitution in sphalerite can occur with and without the need for charge balance by other metal ions, indicating the resilience and flexibility of the sphalerite crystal structure. This study explains the previous observations of multiple ways of Ge incorporation in natural sphalerite, and provides experimental and molecular modeling insight for a better understanding of the processes related to the formation and extraction of Ge in zinc ores.

Declaration of Competing Interest

The authors declare that they have no known competing financial interests or personal relationships that could have appeared to influence the work reported in this paper.

Acknowledgement

Research funding is from the Commonwealth Scientific and Industrial Research Organisation (CSIRO) to W. L., CSIRO's Deep Earth Imaging Future Science Platform to YM, and the Australian Research Council Discovery grant DP220100500 to J.B. The molecular simulation of this work was supported by resources provided by the Pawsey Supercomputing Centre with funding from the Australian Government and the Government of Western Australia, and the high-performance computers in CSIRO. Part of this research was undertaken on the XFM beamline at the Australian Synchrotron, part of ANSTO. We thank Associate Editor Prof. M. Reich, an anonymous reviewer and Dr. A Perez-Fodich for their helpful reviews.

Appendix A. Supplementary material

Supplementary Material includes additional figures, tables and research data related to EPMA, XFM and XANES analysis, ab initio molecular simulations and thermodynamic modeling results. Supplementary material to this article can be found online at https://doi.org/10.1016/j.gca.2022.11.031.

References

Becke, A.D., 1988. Density-functional exchange-energy approximation with correct asymptotic-behavior. Phys. Rev. A38, 3098–3100.
Belissont, R., Boiron, M.-C., Luais, B., Cathelineau, M., 2014. LA-ICP-MS analyses of minor and trace elements and bulk Ge isotopes in zoned Ge-rich sphalerites from the Noailhac – Saint-Salvy deposit (France): Insights into incorporation mechanisms and ore deposition processes. Geochim. Cosmochim. Acta 126, 518–540.
Belissont, R., Muñoz, M., Boiron, M.-C., Luais, B., Mathon, O., 2016. Distribution and oxidation state of Ge, Cu and Fe in sphalerite by μ-XRF and K-edge μ-XANES: insights into Ge incorporation, partitioning and isotopic fractionation. Geochim. Cosmochim. Acta 177, 298–314.
Belissont, R., Munoz, M., Boiron, M.-C., Luais, B., Mathon, O., 2019. Germanium crystal chemistry in Cu-bearing sulfides from Micro-XRF Mapping and Micro-XANES Spectroscopy. Minerals 9, 227.
Bernstein, L.R., 1985. Germanium geochemistry and mineralogy. Geochim. Cosmochim. Acta 49, 2409–2422.
Bethke, C.M., 2007. Geochemical and Biogeochemical Reaction Modeling. Cambridge University Press, Cambridge.
Binnewies, M., Milke, E., 2008 Thermochemical Data of Elements and Compounds: Second, Revised and Extended Edition.
Bonnet, J., Cauzid, J., Testemale, D., Kieffer, I., Proux, O., Lecomte, A., Bailly, L., 2017. Characterization of Germanium Speciation in Sphalerite (ZnS) from Central and Eastern Tennessee, USA, by X-ray Absorption Spectroscopy. Minerals 7, 79.
Brugger, J., McPhail, D.C., Wallace, M., Waters, J., 2003. Formation of willemite in hydrothermal environments. Econ. Geol. 98, 819–835.
Bühl, M., 2009. Structure and stability of aquotetrafluorouranyl(VI) in the solid state - density functional study of UO2F4(H2O) [NMe4]2•2H2O. Can. J. Chem. Revue Canadienne De Chimie 87, 818–823.
Car, R., Parrinello, M., 1985. Unified approach for molecular dynamics and density-functional theory. Phys. Rev. Lett. 55, 2471–2474.
Cook, N.J., Ciobanu, C.L., Pring, A., Skinner, W., Shimizu, M., Danyushevsky, L., Saini-Eidukat, B., Melcher, F., 2009. Trace and minor elements in sphalerite: A LA-ICPMS study. Geochim. Cosmochim. Acta 73, 4761–4791.

Cook, N.J., Ciobanu, C.L., Brugger, J., Etschmann, B., Howard, D.L., de Jonge, M.D., Ryan, C., Paterson, D., 2012. Determination of the oxidation state of Cu in substituted Cu-In-Fe-bearing sphalerite via μ-XANES spectroscopy. Am. Mineral. 97, 476–479.
Cook, N.J., Etschmann, B., Ciobanu, C.L., Geraki, K., Howard, D.L., Williams, T., Rae, N., Pring, A., Chen, G., Johannessen, B., Brugger, J., 2015. Distribution and Substitution mechanism of Ge in a Ge-(Fe)-bearing sphalerite. Minerals 5, 117–132.
Cooke, D.R., Bull, S.W., Large, R.R., McGoldrick, P.J., 2000. The importance of oxidized brines for the formation of Australian Proterozoic stratiform sediment-hosted Pb-Zn (sedex) deposits. Econ. Geol. 95, 1–17.
Cugerone, A., Cenki-Tok, B., Oliot, E., Munoz, M., Barou, F., Motto-Ros, V., Le Goff, E., 2020. Redistribution of germanium during dynamic recrystallization of sphalerite. Geology 48, 236–241.
Dickinson, T., Taylor, G.J., Keil, K., Bild, R.W., 1989. Germanium abundances in lunar basalts: evidence of mantle metasomatism? In: Proceedings of the 19th Lunar and Planetary Science Conference, pp. 189–198.
Ellis, A.J., Giggenbach, W., 1971. Hydrogen sulphide ionization and sulphur hydrolysis in high temperature solution. Geochim. Cosmochim. Acta 35, 247–260.
Etschmann, B., Ryan, C., Brugger, J., Kirkham, R., Hough, R., Moorhead, G., Siddons, D., De Geronimo, G., Kuczewski, A., Dunn, P., Paterson, D., de Jonge, M., Howard, D., Davey, P., Jensen, M., 2010. Reduced As components in highly oxidized environments: Evidence from full spectral XANES imaging using the Maia massively parallel detector. Am. Mineral. 95, 884–887.
Etschmann, B., Brugger, J., Pearce, M.A., Ta, C., Brautigan, D., Jung, M., Pring, A., 2014a. Grain boundaries as microreactors during reactive fluid flow: experimental dolomitization of a calcite marble. Contrib. Miner. Petrol. 168.
Etschmann, B.E., Donner, E., Brugger, J., Howard, D.L., de Jonge, M.D., Paterson, D., Naidu, R., Scheckel, K.G., Ryan, C.G., Lombi, E., 2014b. Speciation mapping of environmental samples using XANES imaging. Environ. Chem. 11, 341–350.
Etschmann, B.E., Liu, W., Li, K., Dai, S., Reith, F., Falconer, D., Kerr, G., Paterson, D., Howard, D., Kappen, P., Wykes, J., Brugger, J., 2017. Enrichment of germanium and associated tungsten and arsenic in coal and roll-front U deposits. Chem. Geol. 463, 29–49.
Etschmann, B.E., Mei, Y., Liu, W., Sherman, D., Testemale, D., Müller, H., Rae, N., Kappen, P., Brugger, J., 2018. The role of Pb(II) complexes in hydrothermal mass transfer: An X-ray absorption spectroscopic study. Chem. Geol. 502, 88–106.
Evans, M.J., Derry, L.A., 2002. Quartz control of high germanium/silicon ratios in geothermal waters. Geology 30, 1019–1022.
Fernandez, N.M., Perez-Fodich, A., Derry, L.A., Druhan, J.L., 2021. A first look at Ge/Si partitioning during amorphous silica precipitation: Implications for Ge/Si as a tracer of fluid-silicate interactions. Geochim. Cosmochim. Acta 297, 158–178.
Filimonova, O.N., Trigub, A.L., Tonkacheev, D.E., Nickolsky, M.S., Kvashnina, K.O., Chareev, D.A., Chaplygin, I.V., Kovalchuk, E.V., Lafuerza, S., Tagirov, B.R., 2019. Substitution mechanisms in In-, Au-, and Cu-bearing sphalerites studied by X-ray absorption spectroscopy of synthetic compounds and natural minerals. Mineral. Mag. 83, 435–451.
Frenzel, M., Hirsch, T., Gutzmer, J., 2016. Gallium, germanium, indium, and other trace and minor elements in sphalerite as a function of deposit type — A meta-analysis. Ore Geol. Rev. 76, 52–78.
George, L.L., Cook, N.J., Ciobanu, C.L., 2016. Partitioning of trace elements in co-crystallized sphalerite–galena–chalcopyrite hydrothermal ores. Ore Geol. Rev. 77, 97–116.
Goldmann, S., Junge, M., Wirth, R., Schreiber, A., 2019. Distribution of trace elements in sphalerite and arsenopyrite on the nanometre-scale – discrete phases versus solid solution. Eur. J. Mineral. 31, 325–333.
Harrowfield, I.R., MacRae, C.M., Wilson, N.C., 1993. Chemical imaging in electron microprobes. Microbeam Anal. 2, 547–548.
Hens, T., Brugger, J., Etschmann, B., Paterson, D., Brand, H.E.A., Whitworth, A., Frierdich, A.J., 2019. Nickel exchange between aqueous Ni(II) and deep-sea ferromanganese nodules and crusts. Chem. Geol. 528, 119276. 13 pp..
Holloway, C.E., Melnik, M., 2001. Germanium coordination compounds: Classification and analysis of crystallographic and structural data. Main Group Met. Chem. 24, 681–726.
Howard, D.L., de Jonge, M.D., Afshar, N., Ryan, C.G., Kirkham, R., Reinhardt, J., Kewish, C.M., McKinlay, J., Walsh, A., Divitcos, J., Basten, N., Adamson, L., Fiala, T., Sammut, L., Paterson, D.J., 2020. The XFM beamline at the Australian Synchrotron. J. Synchrotron Radiat. 27, 1447–1458.
Johan, Z., 1988. Indium and germanium in the structure of sphalerite: an example of coupled substitution with copper. Mineral. Petrol. 39, 211–229.
Keller, P., Anderson, C., 2018. The production of critical materials as by products. Aspects Min Miner Sci. 2 (2). AMMS.000532. 4/14.
Kelley, K.D., Jennings, S., 2004. A special issue devoted to barite and Zn-Pb-Ag deposits in the red dog district, Western Brooks Range, Northern Alaska. Econ. Geol. 99, 1267–1280.
Kelley, K.D., Leach, D.L., Johnson, C.A., Clark, J.L., Fayek, M., Slack, J.F., Anderson, V.M., Ayuso, R.A., Ridley, W.I., 2004. Textural, Compositional, and Sulfur Isotope Variations of Sulfide Minerals in the Red Dog Zn-Pb-Ag Deposits, Brooks Range, Alaska: Implications for Ore Formation. Econ. Geol. 99, 1509–1532.
Leach, D.L., Bradley, D.C., Huston, D., Pisarevsky, S.A., Taylor, R.D., Gardoll, S.J., 2010a. Sediment-Hosted Lead-Zinc Deposits in Earth History. Econ. Geol. 105, 593–625.
Leach, D.L., Taylor, R.D., Fey, D.L., Diehl, S.F., Saltus, R.W., 2010. A deposit model for Mississippi Valley-Type lead-zinc ores: Chapter A in Mineral deposit models for resource assessment. Scientific Investigations Report 2010-5070-A, U.S. Geological Survey, 53 pp.
Lee, C.T., Yang, W.T., Parr, R.G., 1988. Development of the colle-salvetti correlation-energy formula into a functional of the electron-density. Phys. Rev. B 37, 785–789.
Li, K., Etschmann, B., Rae, N., Reith, F., Ryan, C.G., Kirkham, R., Howard, D., Rosa, D.R. N., Zammit, C., Pring, A., Ngothai, Y., Hooker, A., Brugger, J., 2016. Ore petrography using megapixel X-ray imaging: rapid insights into element distribution and mobilization in complex Pt and U-Ge-Cu Ores. Econ. Geol. 111, 487–501.
Li, Z., Ye, L., Hu, Y., Wei, C., Huang, Z., Yang, Y., Danyushevsky, L., 2020. Trace elements in sulfides from the Maozu Pb-Zn deposit, Yunnan Province, China: Implications for trace-element incorporation mechanisms and ore genesis. Am. Mineral. 105, 1734–1751.
Liu, W., Mei, Y., Etschmann, B., Brugger, J., Pearce, M., Ryan, C.G., Borg, S., Wykes, J., Kappen, P., Paterson, D., Boesenberg, U., Garrevoet, J., Moorhead, G., Falkenberg, G., 2017. Arsenic in hydrothermal apatite: Oxidation state, mechanism of uptake, and comparison between experiments and nature. Geochim. Cosmochim. Acta 196, 144–159.
Liu, W., Spinks, S.C., Glenn, M., MacRae, C., Pearce, M.A., 2021. How carbonate dissolution facilitates sediment-hosted Zn-Pb mineralization. Geology 49, 1363–1368.
MacRae, C.M., Wilson, N.C., Torpy, A., 2013. Hyperspectral cathodoluminescence. Mineral. Petrol. 107, 429–440.
Málek, J., Mitsuhashi, T., Ohashi, N., Taniguchi, Y., Kawaji, H., Atake, T., 2011. Heat capacity and thermodynamic properties of germanium disulfide at temperatures from T=(2 to 1240)K. J. Chem. Thermodyn. 43, 405–409.
Mare, E.R., O'Neill, H.S.C., Berry, A.J., Glover, C.J., 2020. The stability of divalent Ge in silicate melts and its geochemical properties. Chem. Geol. 532, 14 pp.
Mei, Y., Sherman, D.M., Liu, W., Etschmann, B., Testemale, D., Brugger, J., 2015. Zinc complexation in chloride-rich hydrothermal fluids (25–600 degrees C): A thermodynamic model derived from ab initio molecular dynamics. Geochim. Cosmochim. Acta 150, 265–284.
Mudd, G.M., Werner, T.T., Weng, Z.-H., Yellishetty, M., Yuan, Y., McAlpine, S.R.B., Skirrow, R., Czarnota K., 2018. Critical Minerals in Australia: A Review of Opportunities and Research Needs. Record 2018/51. Geoscience Australia, Canberra.
Nassar, N.T., Graedel, T.E., Harper, E.M., 2015. By-product metals are technologically essential but have problematic supply. Sci. Adv. 1, e1400180.
Pankratz, L.W., Mah, A.D., Watson, S.W., 1987. Thermodynamic Properties of Sulfides.
Perez-Fodich, A., Derry, L.A., 2020. A model for germanium-silicon equilibrium fractionation in kaolinite. Geochim. Cosmochim. Acta 288, 199–213.
Pokrovski, G.S., Roux, J., Hazemann, J.-L., Testemale, D., 2005. An X-ray absorption spectroscopy study of argutite solubility and aqueous Ge(IV) speciation in hydrothermal fluids to 500 °C and 400 bar. Chem. Geol. 217, 127–145.
Pokrovski, G.S., Schott, J., 1998. Thermodynamic properties of aqueous Ge(IV) hydroxide complexes from 25 to 350°C: implications for the behavior of germanium and the Ge/Si ratio in hydrothermal fluids. Geochim. Cosmochim. Acta 62, 1631–1642.
Pring, A., Wade, B., McFadden, A., Lenehan, C.E., Cook, N.J., 2020. Coupled Substitutions of Minor and Trace Elements in Co-Existing Sphalerite and Wurtzite. Minerals 10, 147.
Ryan, C.G., 2000. Quantitative Trace Element Imaging using PIXE and the Nuclear Microprobe. Int. J. Imaging Syst. Technol. 11, 219–230.
Ryan, C.G., Siddons, D.P., Kirkham, R., Dunn, P.A., Kuczewski, A., Moorhead, G., De Geronimo, G., Paterson, D.J., de Jonge, M.D., Hough, R.M., Lintern, M.J., Howard, D.L., Kappen, P., Cleverley, J., 2010b. The New Maia Detector System: Methods For High Definition Trace Element Imaging Of Natural Material. In: Denecke, M.A., Walker, C.T. (Eds.), X-Ray Optics and Microanalysis, Proceedings, pp. 9–17.
Ryan, C.G., Siddons, D.P., Moorhead, G., Kirkham, R., De Geronimo, G., Etschmann, B. E., Dragone, A., Dunn, P.A., Kuczewski, A., Davey, P., Jensen, M., Ablett, J.M., Kuczewski, J., Hough, R., Paterson, D., 2009. High-throughput X-ray fluorescence imaging using a massively parallel detector array, integrated scanning and real-time spectral deconvolution. J. Phys. Conf. Ser. 186. 9th International Conference on X-Ray Microscopy), 3 pp.
Ryan, C.G., Kirkham, R., Hough, R.M., Moorhead, G., Siddons, D.P., de Jonge, M.D., Paterson, D.J., De Geronimo, G., Howard, D.L., Cleverley, J.S., 2010a. Elemental X-ray imaging using the Maia detector array: The benefits and challenges of large solid-angle. Nucl. Instrum. Methods Phys. Res. Section a-Accelerat. Spectromet. Detectors Associated Equip. 619, 37–43.
Ryan, C.G., Siddons, D.P., Kirkham, R., Li, Z.Y., de Jonge, M.D., Paterson, D.J., Kuczewski, A., Howard, D.L., Dunn, P.A., Falkenberg, G., Boesenberg, U., De Geronimo, G., Fisher, L.A., Halfpenny, A., Lintern, M.J., Lombi, E., Dyl, K.A., Jensen, M., Moorhead, G.F., Cleverley, J.S., Hough, R.M., Godel, B., Barnes, S.J., James, S.A., Spiers, K.M., Alfeld, M., Wellenreuther, G., Vukmanovic, Z., Borg, S., 2014. Maia X-ray fluorescence imaging: capturing detail in complex natural samples. J. Phys. Conf. Ser. 499, 12 pp.
Saini-Eidukat, B., Melcher, F., Lodziak, J., 2009. Zinc-germanium ores of the Tres Marias Mine, Chihuahua, Mexico. Miner. Deposita 44, 363–370.
Shannon, R.D., 1976. Revised effective ionic radii and systematic studies of interatomic distances in halides and chalcogenides. Acta Crystallogr. A 32, 751–767.
Skinner, B.J., 1961. Unit-cell edges of natural and synthetic sphalerites. Am. Mineral. 46, 1399–1411.

Spinks, S.C., Pearce, M.A., Liu, W., Kunzmann, M., Ryan, C.G., Moorhead, G.F., Kirkham, R., Blaikie, T., Sheldon, H.A., Schaubs, P.M., Rickard, W.D.A., 2021. Carbonate Replacement as the Principal Ore Formation Process in the Proterozoic McArthur River (HYC) Sediment-Hosted Zn-Pb Deposit, Australia. Econ. Geol. 116, 693–718.

Syverson, D.D., Etschmann, B., Liu, W.H., Ram, R., Mei, Y., Lanzirotti, T., Mercadier, J., Brugger, J., 2019. Oxidation state and coordination environment of Pb in U-bearing minerals. Geochim. Cosmochim. Acta 265, 109–131.

Torpy, A., Wilson, N.C., MacRae, C.M., Pownceby, M.I., Biswas, P.K., Rahman, M.A., Zaman, M.N., 2020. Deciphering the Complex Mineralogy of River Sand Deposits through Clustering and Quantification of Hyperspectral X-Ray Maps. Microsc. Microanal. 26, 768–792.

Troullier, N., Martins, J.L., 1991. Efficient pseudopotentials for plane-wave calculations. Phys. Rev. B 43, 1993–2006.

USGS, (2020) Mineral Commodity Summaries: https://www.usgs.gov/centers/nmic/mineral-commodity-summaries.

Vaughan, D.J., Corkhill, C.L., 2017. Mineralogy of Sulfides. Elements 13, 81–87.

Wilkinson, J., 2014. Sediment-Hosted Zinc-Lead Mineralization: Processes and Perspectives. Treatise on Geochemistry: Second Edition Chapter 13, 219–249.

Xia, F., Brugger, J., Chen, G., Ngothai, Y., O'Neill, B., Putnis, A., Pring, A., 2009. Mechanism and kinetics of pseudomorphic mineral replacement reactions: A case study of the replacement of pentlandite by violarite. Geochim. Cosmochim. Acta 73, 1945–1969.

Xing, Y., Brugger, J., Zhong, R., Shvarov, Y., 2019. Arsenic evolution as a tool for understanding formation of pyritic gold ores. Geology 47, 335–338.

Ye, L., Cook, N.J., Ciobanu, C.L., Yuping, L., Qian, Z., Tiegeng, L., Wei, G., Yulong, Y., Danyushevskiy, L., 2011. Trace and minor elements in sphalerite from base metal deposits in South China: A LA-ICPMS study. Ore Geol. Rev. 39, 188–217.